





## RESEARCH ARTICLE

10.1029/2025MS005284

# The Effects of Sea-State-Dependent Surface Fluxes on CESM2 Climate Simulations

Xiaoming Shi<sup>1,2</sup> , Qing Li<sup>2,3</sup> , Diah Valentina Lestari<sup>4</sup> , Shangfei Lin<sup>5</sup> , and Hui Su<sup>6</sup> 

## Key Points:

- A sea-state dependent surface flux parameterization is implemented in the Community Earth System Model version 2
- The new scheme reduces biases in the mean climate state such as barotropic jet speed in the Southern Hemisphere and sea surface temperature
- The scheme also produces the weak cooling in some regions of the Pacific, similar to observed trends in recent decades

## Supporting Information:

Supporting Information may be found in the online version of this article.

## Correspondence to:

X. Shi,  
[shixm@ust.hk](mailto:shixm@ust.hk)

## Citation:

Shi, X., Li, Q., Lestari, D. V., Lin, S., & Su, H. (2025). The effects of sea-state-dependent surface fluxes on CESM2 climate simulations. *Journal of Advances in Modeling Earth Systems*, 17, e2025MS005284. <https://doi.org/10.1029/2025MS005284>

Received 7 JUN 2025  
Accepted 17 NOV 2025

<sup>1</sup>Division of Environment and Sustainability, Hong Kong University of Science and Technology, Hong Kong, Hong Kong, <sup>2</sup>Center for Ocean Research in Hong Kong and Macau, Hong Kong University of Science and Technology, Hong Kong, Hong Kong, <sup>3</sup>Earth, Ocean and Atmospheric Sciences Thrust, Hong Kong University of Science and Technology (Guangzhou), Guangzhou, China, <sup>4</sup>School of Civil and Environmental Engineering, Nanyang Technological University, Singapore, Singapore, <sup>5</sup>College of Harbour, Coastal and Offshore Engineering, Hohai University, Nanjing, China, <sup>6</sup>Department of Civil and Environmental Engineering, Hong Kong University of Science and Technology, Hong Kong, Hong Kong

**Abstract** Processes at the air-sea interface govern the climate mean state and variability by determining the exchange of momentum, heat, and water between the atmosphere and ocean. Traditional climate models compute those exchanges across the air-sea interface by assuming an ocean surface with roughness determined by atmospheric wind and stability conditions, essentially assuming ocean surface waves are in equilibrium states. In reality, that is rarely the case. Such effects have been emphasized in numerical weather predictions for weather systems like tropical cyclones. An accurate representation of ocean surface waves requires a prognostic ocean surface wave model. The addition of WAVEWATCH III to the Community Earth System Model version 2 (CESM2) makes it possible to parameterize the impacts of ocean surface waves on the momentum and energy exchange. This study documents the implementation of a sea-state-dependent surface flux scheme in CESM2. It considers the effects of waves on ocean surface roughness and those of sea spray on sensible and latent heat. It is found that the new scheme significantly impacts mean atmospheric circulation and the upper ocean. The errors in mean atmospheric circulation and surface temperature patterns are reduced. The modified surface flux lowers the eddy-driven jet speed and weakens the Hadley circulation. Global sea surface temperature (SST) warm bias is reduced due to the cooling of the Southern Ocean and eastern boundary currents. In particular, some parts of eastern and central Pacific exhibit a weak cooling trend in the simulation for recent decades, reducing the existing SST trend bias in CESM2.

**Plain Language Summary** The ocean and the atmosphere are both essential components of the Earth system. They exchange momentum, heat, and water at the air-sea interface. Traditionally, those exchanges are estimated based on atmospheric stability, wind, and the air-sea difference in temperature and humidity, which are assumed to determine microscale turbulence. Ocean surface waves can potentially change the morphology of the air-sea interface and, therefore, affect turbulence. Sea spray generated in waves can also enhance water vapor transport into the atmosphere via the evaporation of small droplets. However, those enhancements depend on sea states such as wave height and phase speed, which were traditionally not simulated in Earth system models. The WAVEWATCH III model has recently been added to the Community Earth System Model version 2 (CESM2) to compute sea states and improve ocean surface mixing. In this work, we developed a new scheme in CESM2 to include the effects of ocean surface waves on air-sea momentum, heat, and water exchanges. We found that the new methods reduce lower-level wind speed in the atmosphere and introduce meaningful improvements in temperature, precipitation, and ocean circulation. The improved sea-state dependent air-sea coupling in CESM2 can yield more realistic climate simulations regarding the mean states and trends.

## 1. Introduction

The ocean and atmosphere coupling is critical in the Earth system. It determines the development of short-term weather phenomena and modulates low-frequency climate variabilities. For instance, tropical cyclones (TCs) draw energy from the ocean through sea surface enthalpy flux (Emanuel, 1986), and previous studies from world-leading numerical weather prediction agencies have demonstrated that atmosphere-ocean coupling plays an essential role in TC intensity prediction (Bernardet et al., 2015; Mogensen et al., 2017; Wada et al., 2018; Yu et al., 2013). TC intensity errors in the ECMWF Reanalysis version 5 (ERA5) have also been found to correlate

with its bias in surface enthalpy flux (Zhao et al., 2022). For climate projections, lacking atmosphere-ocean coupling can limit a climate model's skills in simulating natural climate variability (Barsugli & Battisti, 1998; He & Soden, 2016). Such influences are especially notable for El Niño-Southern Oscillation (ENSO), Asia monsoon, and temperature and precipitation extremes (Fischer et al., 2018; Hirons et al., 2018; Newman et al., 2009; Zhu & Shukla, 2013).

The exchange of momentum, enthalpy, aerosols, and CO<sub>2</sub> governs the influence of atmosphere-ocean coupling. What complicates this coupling is the existence of ocean surface gravity waves, which can modify ocean surface roughness, generate sea spray, and induce Langmuir mixing in the ocean surface boundary layer, among other effects (Cavaleri et al., 2012). Comparison of simulations with direct measurements from the Coupled Boundary Layer Air-Sea Transfer field experiment suggests that reanalysis products substantially underestimate latent heat flux under TC conditions, and including surface wave-related effects can reduce such bias (J. Liu et al., 2011). Meanwhile, including ocean-atmosphere-wave coupling has been found effective in improving wind and wave simulation accuracy (Olabarrieta et al., 2012). A few regional ocean-atmosphere-wave coupled models have been developed and evaluated in TC simulations, and the dependency on sea state helps those models improve the simulated TC intensity and structure (S. S. Chen et al., 2013; Pianezze et al., 2018; Warner et al., 2010; Zhao et al., 2022). Besides high wind conditions, the misalignment between swell direction and wind complicates wind stress estimation, influencing both wind speeds and momentum flux distributions in the planetary boundary layer (PBL) (Wu et al., 2024). Some studies introduced swell-related mixing length scales into PBL parameterizations (Nilsson et al., 2012; Rutgersson et al., 2012; Wu et al., 2017).

However, the effects of ocean waves on air-sea interaction in Earth system models are only considered in limited studies. Song et al. (2012) coupled the marine science and numerical modeling (MASNUM) surface wave model with the ocean component of the Community Climate System Model Version 3 (CCSM3) to represent non-breaking wave-induced vertical mixing, and they found tropical SST was much improved. Qiao et al. (2013) coupled the MASNUM wave model with other components in the First Institute of Oceanography-Earth System Model (FIO-ESM), which was the first to include surface waves among all the climate models participating in the Coupled Model Intercomparison Project Phase 5 (CMIP5). Using a coupled atmosphere-wave model, Shimura et al. (2017) evaluated how wave-dependent estimation of sea surface roughness may influence the mean climate state in their simulations and found tropical winds are enhanced, which leads to significant changes in the Hadley circulation. Bao et al. (2020) developed FIO-ESM v2.0, which included the effect of surface wave Stokes drifts on air-sea momentum and heat fluxes and wave-induced sea spray on air-sea heat fluxes. In particular, FIO-ESM v2.0 reduced the significant warm bias of SST near the eastern boundary of the tropical Pacific in FIO-ESM v1.0, a common challenge for all climate models (Bao et al., 2020). Lee et al. (2021) assessed all 59 CMIP6 climate models regarding their skills in reconstructing historical ENSO events, and they found FIO-ESM v2.0 had the best performance.

The recent implementation of WAVEWATCH III (WW3) into the Community Earth System Model (CESM) by Q. Li et al. (2016) provides an excellent opportunity for studying the impact of active ocean-wave-atmosphere coupling on the climate simulation in an Earth system model. Q. Li et al. (2016) demonstrated that biases of ocean mixed layer depth, temperature, and ocean ventilation are effectively reduced by parameterizing the Langmuir mixing based on sea state. Active atmosphere-wave coupling, or more precisely, surface flux-wave coupling, was not included in CESM yet. Conventional approaches relate surface fluxes of momentum, heat, and moisture to the air-sea gradient of wind, temperature, and moisture mixing ratio. Introducing sea-state dependence allows a more accurate calculation of the fluxes and, therefore, a better representation of the air-sea interaction in the presence of waves.

In this study, we implement a sea-state-dependent sea surface roughness length parameterization and add sea spray-induced fluxes into CESM2 (Danabasoglu et al., 2020). We describe the details of the parameterization and its implementation in Section 2. In Sections 3 and 4, we describe the impact of the new parameterization on the simulated surface fluxes and climate states, respectively. We summarize our main findings in Section 5, together with a brief discussion on the limitations and implications of this study, an effort towards a full ocean-atmosphere-wave coupling in Earth system modeling.

## 2. Methods and Experiments

### 2.1. Wave-Dependent Fluxes

The original CESM2 bulk formulas for turbulence fluxes of momentum ( $\tau$ ), water ( $E$ ), and sensible heat ( $H$ ) are the following (Neale et al., 2010),

$$\tau = \rho_A |\Delta \mathbf{V}| C_D \Delta \mathbf{V} \quad (1)$$

$$E = \rho_A |\Delta \mathbf{V}| C_E \Delta q \quad (2)$$

$$H = \rho_A |\Delta \mathbf{V}| C_H \Delta \theta \quad (3)$$

where  $\rho_A$  is surface air density,  $C_p$  is the specific heat of air at constant pressure,  $\Delta \mathbf{V} = \mathbf{V}_A - \mathbf{V}_s$  is the velocity difference between the wind of the lowest atmospheric model level and ocean surface current,  $\Delta \theta = \theta_A - T_s$  is the difference between the potential temperature at the lowest atmospheric model level and SST, and  $\Delta q = q_A - q_s(T_s)$  is the difference between the specific humidity at the lowest model level and the surface saturation specific humidity at the SST. The transfer coefficients,  $C_D$ ,  $C_E$ , and  $C_H$ , are functions of stability  $\zeta$  and the momentum roughness length  $Z_0$ . For example,

$$C_D = \kappa^2 \left[ \ln \left( \frac{Z_A}{Z_0} \right) - \psi_m \right]^{-2} \quad (4)$$

where  $\kappa = 0.4$  is von Kármán's constant,  $Z_A$  is the height of the lowest model level, and  $\psi_m = \psi_m(\zeta)$  is the integrated flux profiles for momentum. The transfer coefficients themselves depend on surface fluxes. The system of equations is solved by iteration.

#### 2.1.1. Wave-Dependent Roughness

Our first modification of the surface exchange formulations is updating the momentum roughness. In the original CESM2,

$$Z_0 = 10 \exp \left[ -\kappa \left( \frac{c_4}{U_{10}} + c_5 + c_6 U_{10} \right)^{-1} \right] \quad (5)$$

where  $c_4 = 2.7 \times 10^{-3} \text{ m s}^{-1}$ ,  $c_5 = 1.42 \times 10^{-4}$ , and  $c_6 = 7.64 \times 10^{-5} \text{ m}^{-1} \text{ s}$  are fitting coefficients,  $\kappa$  is von Kármán constant, and  $U_{10}$  is the 10-m wind speed which depends on stability and the neutral condition 10-m drag coefficient

$$C_{10}^N = c_4 U_{10}^{-1} + c_5 + c_6 U_{10} \quad (6)$$

The unit of  $Z_0$  is meters.

Our new formulation follows Lin et al. (2021). The sea surface roughness is decomposed to a smooth flow component  $Z_0^s$  due to viscosity and rough flow component  $Z_0^r$  that is driven by surface gravity waves,

$$Z_0 = Z_0^s + Z_0^r \quad (7)$$

The smooth flow component is given as Fairall et al. (2003)

$$Z_0^s = 0.11 \nu / u_* \quad (8)$$

where  $\nu$  is the kinematic viscosity of the air and  $u_*$  is the air-side friction velocity. The rough flow component is given by Lin et al. (2021) is

$$Z'_0 = \begin{cases} 4.54H_s(c_p/u_*)^{-3.90}, & c_p/u_* < 12 \\ 5.61 \times 10^{-3}H_s(c_p/u_*)^{-1.20}, & 12 \leq c_p/u_* < 30 \\ 1.57 \times 10^{-5}H_s(c_p/u_*)^{0.50}, & c_p/u_* \geq 30 \end{cases} \quad (9)$$

which is a function of significant wave heights  $H_s$  and wave age,  $c_p/u_*$ , with  $c_p$  being the peak phase speed of waves. Following Davis et al. (2008), we capped the sea surface roughness at  $2.85 \times 10^{-3}$  m in our model, which is widely adopted in the modeling community.

In this parameterization, the roughness length has different relations with the wave age under wind-sea-dominated, mixed, and swell-dominated sea states. This setting is configured according to Lin and Sheng (2020, LS20). The drag coefficient suggested by LS20 was developed based on a set of observational data from eight field experiments across the Atlantic and Pacific Oceans, as summarized in Table S1 in Supporting Information S1. The observed fetches and wave ages listed in Table S1 in Supporting Information S1 have a wide range of values, indicating the complexity of sea states ranging from wind-sea-dominated to swell-dominated states. Many other schemes assume the normalized roughness as a function of wave age or steepness (e.g., Drennan et al., 2003; Edson et al., 2013; Taylor & Yelland, 2001). However, these schemes were mostly developed based on data under wind-sea-dominated conditions and may not be appropriate under swell-dominated sea states (Drennan et al., 2005; Edson et al., 2013). The widely used COARE 3.5 scheme assumes the Charnock parameter as a function of wind speed and does not account for the wave impacts explicitly (Edson et al., 2013). Compared with nine different schemes, including the widely used COARE 3.5, LS20 better represents the drag coefficient from low to high winds (Figure S1a in Supporting Information S1, in which only some schemes are shown and more details were presented in LS20). The increasing wave age in swell-dominated sea states, which corresponds to enhanced drag coefficient at low winds, is mostly due to the effect of opposing swell and is associated with the wind gustiness (García-Nava et al., 2009; Lin & Sheng, 2020; Potter, 2015). The opposing swell can enhance the drag coefficient and the effective sea surface roughness. Therefore, the predicted values of the friction velocity in LS20 spread close to the perfect-fitting line, rather than scattering in others (Figure S1b in Supporting Information S1). In fact, the most distinct swell pools are located in the regions off the west coast of Australia and the Americas. In both regions, the mean wave directions are from the west or south, affected by swell propagating from the Southern Ocean (G. Chen et al., 2002; Young, 1999), while the mean wind stress is in the easterly trade wind belts with relatively consistent east to south-east winds. Therefore, the use of LS20 can well present the enhanced drag coefficient in these regions under opposing swell. This new formula was demonstrated to have good performance in calculating air-sea flux and thus waves, currents, and storms in the South China Sea (Z. Li et al., 2024) and the Atlantic (Lin et al., 2021).

To implement this new parameterization of surface roughness length for surface fluxes in CESM2, we modified the code of the coupler in CESM2 to receive the significant wave height  $H_s$  and peak wave phase speed  $c_p$  from WW3. In the coupler, the original Equation 5 is replaced by Equations 7–9 when computing surface fluxes. It should be noted that some studies chose to update the Charnock parameter as a function of sea state (e.g., Janssen, 2004; B. Liu et al., 2012). In particular, the scheme developed by Janssen (1989), Janssen (1991, 2004) relates the Charnock parameter to the full-spectrum integrated stress induced by waves. It is well-tested and allows the atmosphere to respond quickly to a changing sea state. However, the default CESM2 surface flux scheme does not involve using a Charnock parameter (Neale et al., 2010). Thus, updating the roughness length appears to be a more consistent option with the existing code. Others also adopt such practice in the literature (e.g., Prakash et al., 2019). In the future, it would be interesting to compare our implementation with alternative parameterizations.

### 2.1.2. Sea Spray-Induced Fluxes

Sea spray droplets are generated due to wave breaking. In most situations, the evaporation of those droplets enhances latent flux and reduces sensible heat to the atmosphere. Based on cloud microphysics, a bulk microphysical model was developed to calculate the sea spray-induced sensible and latent heat fluxes (Andreas, 1989, 1990, 1992, 1995, 1998). However, this bulk model considers a spectrum of droplets with varying sizes and is complex and computationally inefficient.

Andreas et al. (2008) observed that the sea spray-induced latent and sensible flux has a large magnitude for droplets with radii around 50 and 100  $\mu\text{m}$ , respectively. Therefore, they hypothesized that the microphysical behavior of droplets at those radii might be good indicators of sea spray-induced fluxes. With this hypothesis, Andreas et al. (2015) developed a fast spray-flux algorithm, in which the spray-induced moisture flux ( $E_{sp}$ ) and sensible heat flux ( $H_{sp}$ ) are

$$E_{sp} = \rho_w \left\{ 1 - \left[ \frac{r(\tau_{f,50})}{50\mu\text{m}} \right]^3 \right\} V_E(u_*) \quad (10)$$

$$H_{sp} = \rho_w C_w (T_s - T_{eq,100}) V_S(u_*) \quad (11)$$

Here,  $\rho_w$  is seawater density,  $C_w$  is the specific heat of water,  $\tau_{f,50}$  is the residence time of droplets with 50  $\mu\text{m}$  initial radius,  $r(\tau_{f,50})$  is the radius of those droplets when they fall back into the sea, and  $T_{eq,100}$  is the equilibrium temperature of droplets with 100  $\mu\text{m}$  initial radius.  $V_E$  and  $V_S$  are wind functions (with the unit of  $\text{m s}^{-1}$ ) that depend on the friction velocity  $u_*$ ,

$$V_E = \begin{cases} 1.76 \times 10^{-9}, & 0 \leq u_* \leq 0.1358 \\ 2.08 \times 10^{-7} u_*^{2.39}, & u_* > 0.1358 \end{cases} \quad (12)$$

$$V_S = \begin{cases} 3.92 \times 10^{-8}, & 0 \leq u_* \leq 0.1480 \\ 5.02 \times 10^{-6} u_*^{2.54}, & u_* > 0.1480 \end{cases} \quad (13)$$

$\tau_{f,50}$  and  $T_{eq,100}$  depend on wave height from WW3. These equations essentially depend on the radius and temperature changes of sea spray droplets when they settle down from the wave height. Further details about their calculation are provided in Andreas et al. (2015) and references therein.

To incorporate the effects of sea spray-induced fluxes in CESM2, we modify the moisture and sensible heat fluxes in Equations 2 and 3 according to

$$E_T = E - E_{sp} \quad (14)$$

$$H_T = H - H_{sp} \quad (15)$$

where  $E_T$  and  $H_T$  are total moisture and sensible heat fluxes, respectively. Note that negative signs are applied to  $E_{sp}$  and  $H_{sp}$  in the above equations because CESM2 coupler's original fluxes according to Equations 2 and 3 are defined with downward flux (atmosphere-to-ocean) being the positive directions. Adding the sea spray fluxes to the traditional flux parameterization is an approach adopted in some previous studies (e.g., Prakash et al., 2019). When the wave height is zero, the sea spray fluxes diminish. Thus, it appears plausible to add those components together. However, the traditional formulation may implicitly capture spray effects, so fine-tuning of model parameters is needed in future work to improve accuracy and optimize overall climate simulation performance.

## 2.2. Climate Simulations

We implemented the new algorithms above into CESM2 version 2.2.0. Four historical simulations are conducted to evaluate the impact of the new wave-dependent fluxes on the CESM2 simulation,

1. **REF**: using the original CESM2 code without any changes;
2. **MOM**: including the formulation of wave-dependent roughness length calculation, but not the sea spray effects;
3. **FLX**: including both the new roughness length and sea spray-induced fluxes in its code.
4. **TEST**: keeping original surface flux scheme of CESM2 but modify coefficients in Equation 5 to amplify the transfer coefficient for momentum,  $C_D$ .

These parallel experiments differentiate the effects of the new roughness and sea spray flux computation. The TEST simulation is added to evaluate whether the effects on climate by the new surface wave-dependent scheme are primarily due to the increase in the drag coefficient. In the TEST simulation, a factor of 1.5 is multiplied to the right-hand-side of Equation 6 to increase the amplitude of the resulting  $C_D$  artificially.

We conducted fully coupled CESM2 simulations under transient historical forcing. This is the component set (compset) BHIST in CESM2, which supplies both configure and namelist settings for the predefined experiment. The simulation runs from 1850 to 2014. Its initial condition is the 131th year of a preindustrial control simulation. We run the REF simulation for the entire period. The MOM and FLX simulations were branch runs from the REF simulation after 100 years of simulation, running from 1951 to 2014. Throughout this study, if not specified otherwise, we used the last 40 years (1975–2014) of the simulation data for analysis. This allows the three simulations to diverge and is sufficient to illustrate the differences among the three simulations.

The atmosphere and land components run on a latitude-longitude grid of  $1.9^\circ$  by  $2.5^\circ$ . The ocean and sea ice components run on a nominal  $1^\circ$  Greenland Pole grid, which is a latitude-longitude grid, with the North Pole displaced over Greenland to avoid singularity problems in the ocean and ice models. The ocean surface wave component runs on a near-global latitude-longitude grid of  $3.2^\circ$  by  $4.0^\circ$ , with polar caps at  $78^\circ\text{N/S}$ . We acknowledge that the resolution for WW3 is relatively low, which might cause biases in the representation of sea states. However, this is the only supported resolution used in the current version of CESM2. It is probably sufficient for our purposes to demonstrate the influence of sea states on the air-sea fluxes and the climate on a global scale, but it would be beneficial for improving climate simulation fidelity if future versions of CESM can support higher resolutions for WW3.

### 3. Surface Fluxes

Here, we first examine the changes in surface fluxes due to the introduction of sea state dependency. Figure 1 shows the 40-year averaged ocean surface wind stress in the REF simulation with vectors and the change in the magnitude of wind stress relative to REF with color shading. Mid-latitude westerlies and tropical easterlies determine the REF simulation's wind stress pattern. The wind stress on the eastern boundary currents, such as the flow near the western coast of the Americas, has a notable meridional component.

Comparing the MOM and REF simulations, the dominant change in mid- and high-latitudes is the weakening of the westerly wind stress near the Antarctica coast, especially in the Southern Ocean off the West Antarctica coast. Meanwhile, the westerly wind stress in the Southern Ocean around East Antarctica exhibits some strengthening. Subtropical latitudes exhibit enhancement of wind stresses, especially in regions with a significant meridional component, such as the subtropical Atlantic Ocean and the Southern Hemisphere Indian Ocean. However, the equatorial Pacific Ocean exhibits weakening of easterly wind stress. The FLX simulation exhibits similar patterns to MOM, but the reduction of westerly wind stress in the Southern Ocean off West Antarctica and enhancement of westerly stress in the Southern Ocean off East Antarctica are suppressed.

However, the actual change in wind stress can be caused by changes in near-surface wind conditions, the drag coefficient  $C_D$ , or both. Figure 2a shows the time mean and zonal mean of the drag coefficient. At most latitudes, the wave-dependent roughness length caused about 50% increases in the drag coefficient over the ocean surface. Thus, it is clear that if there were no change in wind conditions, we should see an enhancement of wind stress everywhere over the ocean. The weakening in the Southern Ocean, North and Equatorial Pacific, and North Atlantic Ocean is due to weakened near-surface wind conditions. The drag coefficient in the FLX simulation is slightly smaller than that in the MOM simulation, especially in the Southern Ocean, suggesting that the FLX simulation's near-surface condition is marginally more stable. This is probably related to the additional cooling of SST in FLX compared with MOM, which is described in the next section.

Figure 1c shows the difference between the TEST and REF simulations. Similar to MOM and FLX simulations, the drag coefficient in the TEST simulation is substantially enhanced (Figure 2). However, it appears that the changes in mid-latitudes and high latitudes are primarily a result of the increase in surface drag coefficient, while in low latitudes, the changes in TEST are significantly weaker than those in MOM and FLX. For example, in the tropical Atlantic region, wind stress is enhanced substantially in MOM and FLX simulations, but the response is weaker in the TEST simulation. Such differences suggest that changes in low-latitude wind stress characteristics depend more on local surface wave attributes and the corresponding atmospheric wind changes.

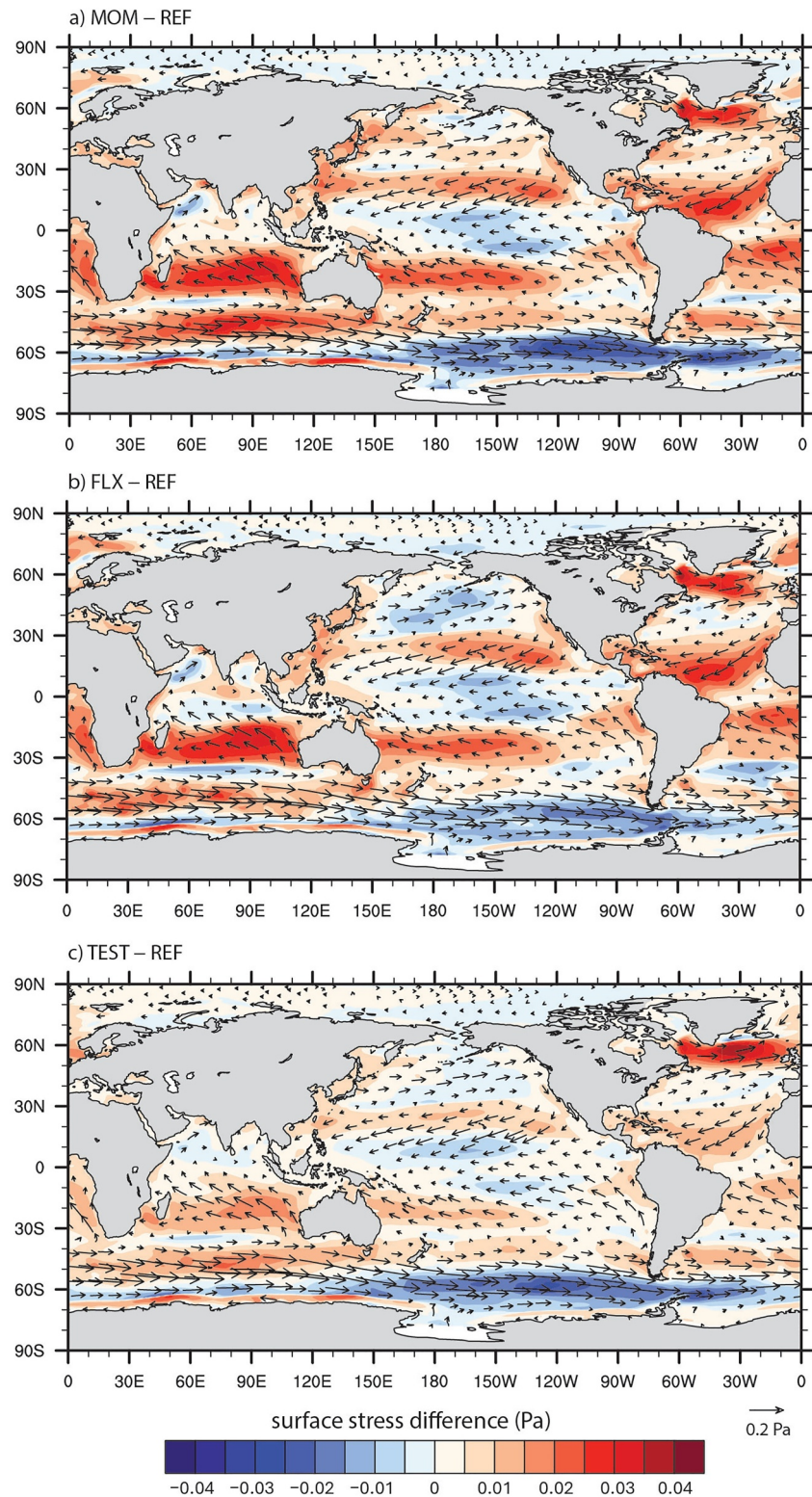


**Figure 1.** Ocean surface wind stress in the REF simulation (vectors) and the difference in stress magnitude (color shading) between (a) MOM and REF, (b) FLX and REF, and (c) TEST and REF simulations. Note that the stress is the momentum flux into the ocean. Data for 1975–2014 are averaged in time for the analysis.

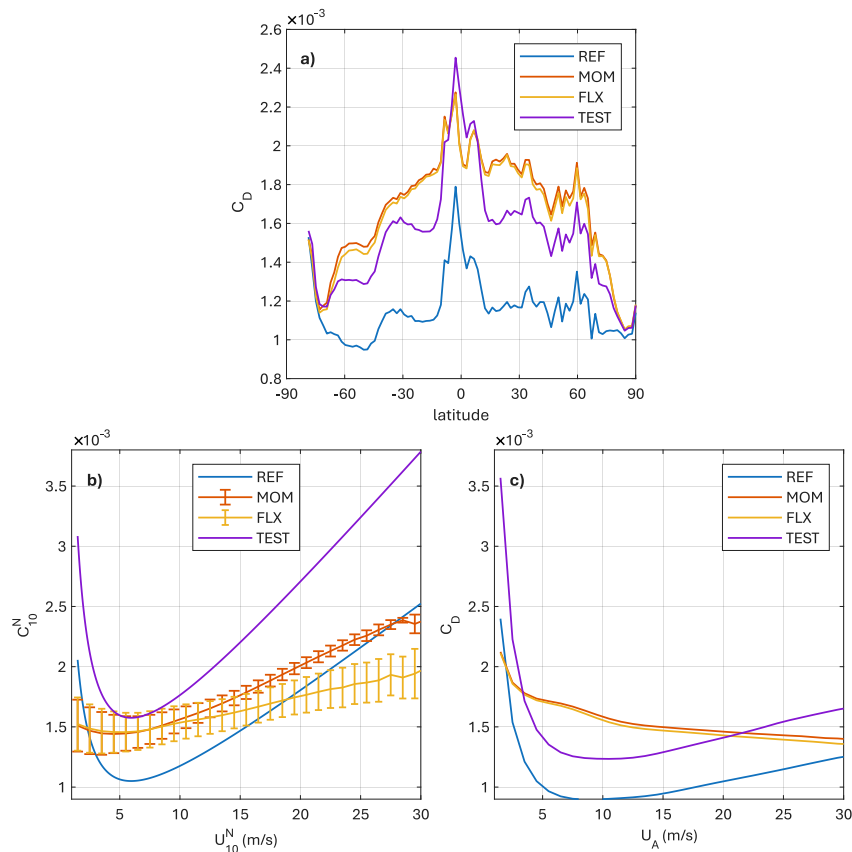


**Figure 2.** (a) Time mean, zonal mean of the momentum transfer coefficient  $C_D$  over the ocean surface in simulations, (b) The dependence of neutral condition, 10-m height transfer coefficient ( $C_{10}^N$  on wind speed ( $U_{10}^N$ )), and (c) actual mean  $C_D$  as a function of wind speed at the lowest model level ( $U_A$ ). In panel (b), error bars are one standard deviation above and below the mean, and the MOM and FLX curves are calculated based on the simulations' sea-state-dependent roughness length and neutral condition expressions, while the REF and TEST curves are based on Equation 6.

It should be noted that the change in MOM and FLX is not simply amplifying the drag coefficient by a constant factor like the design of the TEST simulation. Figure 2b shows the dependence of neutral condition, 10-m level drag coefficient  $C_{10}^N$  on wind speed  $U_{10}^N$  (Edson et al., 2013) in our simulations. At very low wind speed of  $\sim 1 \text{ m s}^{-1}$ , the mean  $C_{10}^N$  in MOM and FLX is actually lower than that in REF and TEST, but for wind speed between  $2 \text{ m s}^{-1}$  and  $18 \text{ m s}^{-1}$ ,  $C_{10}^N$  in MOM and FLX is higher than that in REF. For wind speed higher than  $18 \text{ m s}^{-1}$ ,  $C_{10}^N$  in FLX becomes lower than that in REF, while  $C_{10}^N$  in MOM is still mostly higher than that in REF. Somewhat surprisingly,  $C_{10}^N$  in TEST is higher than that in MOM and FLX, but the actual drag coefficient  $C_D$  in TEST is lower than that in MOM or FLX for moderate wind speed and on average (Figures 2a and 2c). This discrepancy is probably because MOM and FLX do not really use a relation between  $Z_0$  and  $U_{10}^N$  like Equation 5 to solve for  $C_D$ , thus the integrated flux profiles  $\psi_m$  (Equation 4) in REF and TEST differ significantly from those in MOM and FLX for similar wind conditions. In principle, one could define another “TEST” simulation in which the drag coefficient is adjusted by a function of wind speed, rather than a constant. However, such an approach would require multiple trial-and-error experiments to match the relationship between  $C_{10}^N$  and  $U_{10}^N$  in MOM or FLX while matching the climatological mean  $C_D$ .

Figure 3 shows the time mean distribution of significant wave height, peak wave speed, and wave age. Those patterns are consistent with analysis based on global reanalysis data (Hanley et al., 2010). The most energetic wave conditions occur in the Southern Ocean as a result of the extended fetch provided for the high westerly winds. Similar high significant wave heights exist in the North Pacific and North Atlantic Oceans. Peak wave speeds are high in the eastern tropical Pacific, Atlantic, and Indian Ocean, consistent with the observed distribution of swell pools (e.g., G. Chen et al., 2002; Semedo et al., 2011). The high waves in the Southern Ocean and

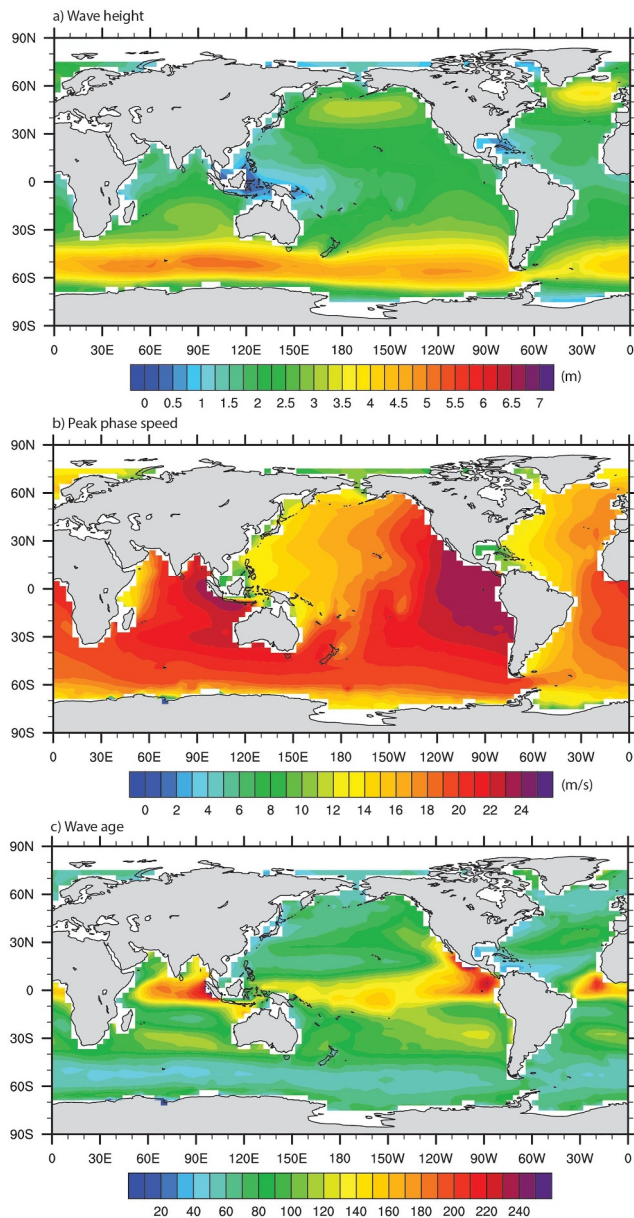


**Figure 3.** Significant wave height  $H_s$  (a), peak wave speed  $C_p$  (b), and wave age  $C_p/u_{*}$  (c) in the FLX simulation. Data for 1975–2014 are averaged in time for the analysis.

The TEST simulation exhibits minimal changes in sensible and latent heat fluxes, especially when compared with the FLX run, suggesting the sea spray effects are relatively independent from the roughness and drag coefficient changes.

## 4. Impacts on Climate States

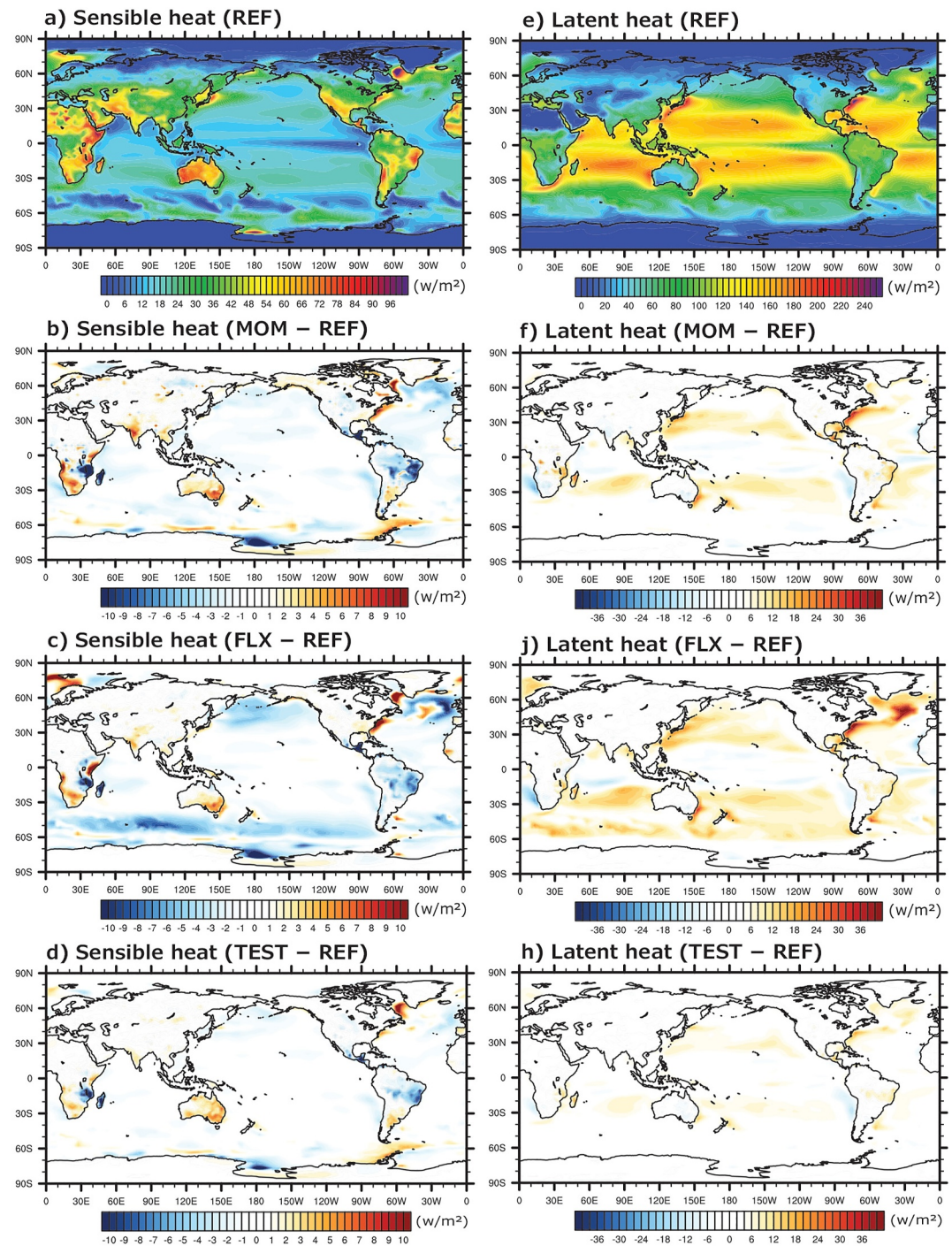
### 4.1. Atmospheric Circulation

Figure 5 compares the climatological mean zonal wind in our simulations with the ERA5 reanalysis (Hersbach et al., 2020). The differences between MOM, FLX, or TEST and the REF simulations are shown in Figure S4 in Supporting Information S1. The REF simulation exhibits large bias at the latitudes of the barotropic jet, especially in the Southern Hemisphere and the stratosphere (Figure 5a). The MOM simulation weakens midlatitude

North Pacific probably generated intense drag to the atmosphere, lowering the climatological mean wind conditions in those regions. In swell-dominated (high wave age) conditions, sea surface roughness increases with wave phase speed (Equation 9). Thus, the enhancement of easterly wind stress in tropical oceans, especially the change in eastern boundary currents, should be partially due to the high wave age in the swell pools. Overall, changes in the wind stress are jointly governed by the wave-dependent roughness and nonlinear response of atmospheric circulation. The former changes the sea surface drag and varies spatially in accordance with wave characteristics. The latter directly modifies the wind speed. The seasonal variations of wave height and phase speed are shown in Figures S2 and S3 in Supporting Information S1, respectively. Wave height exhibits higher values in the winter hemisphere along storm tracks, where wave height values are about 2 m higher than summertime wave height. The phase speed of waves is also higher in the winter hemisphere in general. However, in the India ocean, the boreal summer mean phase speed is about  $5 \text{ m s}^{-1}$  higher than winter mean near Southeast Asian and Australia.

Figure 4 shows the climatological mean surface sensible and latent heat fluxes into the atmosphere in the REF simulation and the changes in MOM and FLX due to introducing the wave-dependent roughness and sea spray-induced fluxes. The MOM simulation has slight decreases in sensible heat flux over most ocean surface areas (Figure 4b). The transfer coefficients for heat fluxes ( $C_H$  and  $C_E$ ) depend not only on the roughness length of latent and sensible heat but also on the roughness length of momentum. It appears that sensible heat flux increased only in the Gulf Stream region. The decrease in sensible heat over the ocean surface is found to be a result of decreases in the near-surface wind (see the next section), which is ubiquitous due to the enhanced momentum drag (Figure 2). However, the change in latent heat flux (Figure 4f) is larger than the magnitude of sensible heat flux. The increase in latent heat flux can be found over the subtropical oceans in the MOM simulation, which does not include the sea spray effect. Therefore, that enhancement is probably due to the change in momentum roughness length and the resulting frictional velocity enhancement. In the FLX simulation, the latent heat flux over the Southern Ocean, North Pacific, and North Atlantic is enhanced, likely due to the effects of the high wind conditions of the storm tracks on waves and sea spray.

The FLX simulation exhibits more decreases in sensible heat flux in the Southern Ocean and North Pacific Ocean than MOM, and we will show in the next section that this is also related to the cooling of the SST in those regions. However, the latent heat flux change is more prominent than the sensible heat flux. Unlike MOM, FLX transfers more latent heat into the Southern Ocean and North Atlantic atmosphere, in which region, wave height is considerable.



**Figure 4.** Total sensible (a–d) and latent (e–h) heat flux into the atmosphere in the simulations. All data are averaged in time from 1975 to 2014. Panels (a) and (e) show the time mean sensible and latent heat flux for the REF simulation. Panels (b), (f) are for the differences between MOM and REF simulations, (c) and (j) for FLX and REF, (d) and (h) for TEST and REF.

westerlies and tropical easterlies in the lower troposphere, thereby reducing the wind biases (Figure 5b). The upper-level subtropical jet enhances as the midlatitude barotropic jet weakens. Because the Eliassen-Palm fluxes produced by baroclinic eddies propagate wave activities equatorward and upward, which decelerate the upper-level subtropical jet and accelerate mid-latitude low-level westerlies (Vallis, 2017), the change in Figure 5 implies that baroclinic eddy activities are suppressed in the MOM simulation due to the enhanced surface drag.

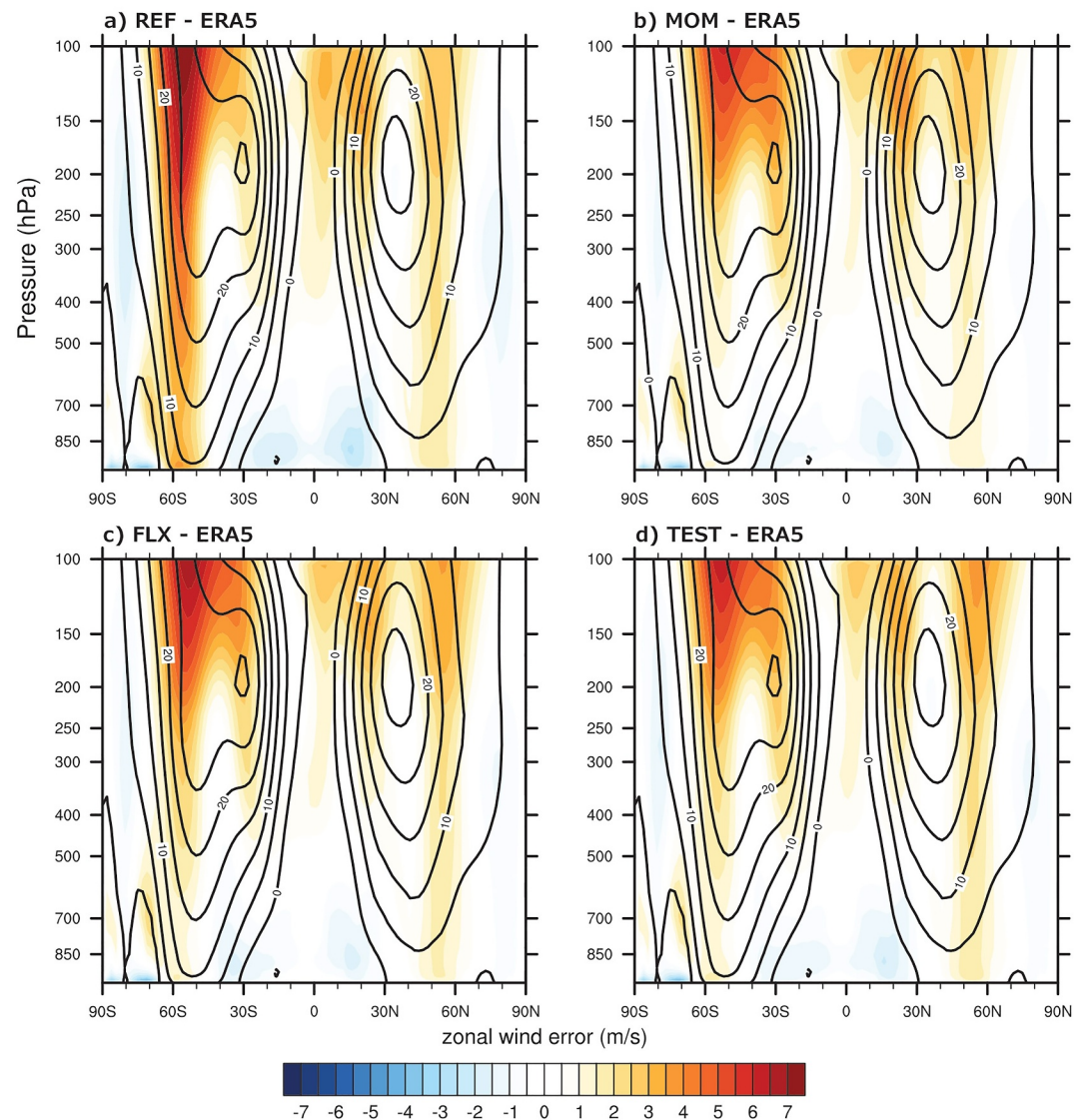


**Figure 5.** Time mean, zonal mean zonal wind in the simulations and observation. Contours are temporally and zonally averaged zonal wind in the ERA5 reanalysis, and color shading indicates differences between the CESM2 simulations and ERA5.

Previous studies indeed found that enhanced surface drag can reduce globally averaged eddy kinetic energy (Barnes & Garfinkel, 2012; Garfinkel et al., 2013). The stratosphere jet bias shows little improvement, probably because the bias source is the relatively low model top in CESM2 and cannot be affected by lower-level changes.

The FLX simulation exhibits reduced bias compared with the REF simulation, but it has a slightly larger bias than the MOM simulation in terms of the Southern Hemisphere barotropic jet (Figure 5c and Figure S4b in Supporting Information S1). Given that the main difference between FLX and MOM simulations is the enhanced latent heat flux in the Southern Ocean and over the western boundary currents regions, the difference in zonal wind suggests the increased latent heat flux has the effect of enhancing baroclinic storms, which are the key to the strength of the barotropic jets. The TEST simulation exhibits a pattern similar to those of the MOM and FLX simulations, suggesting that the change in mean zonal wind is dominated by increased surface drag. However, careful examination reveals that the TEST simulation exhibits less reduction of low level tropical easterly wind bias (Figure 5d and Figure S4c in Supporting Information S1). Thus, this difference again suggests low-latitude dynamical changes are not a simple result of enhanced surface drag.

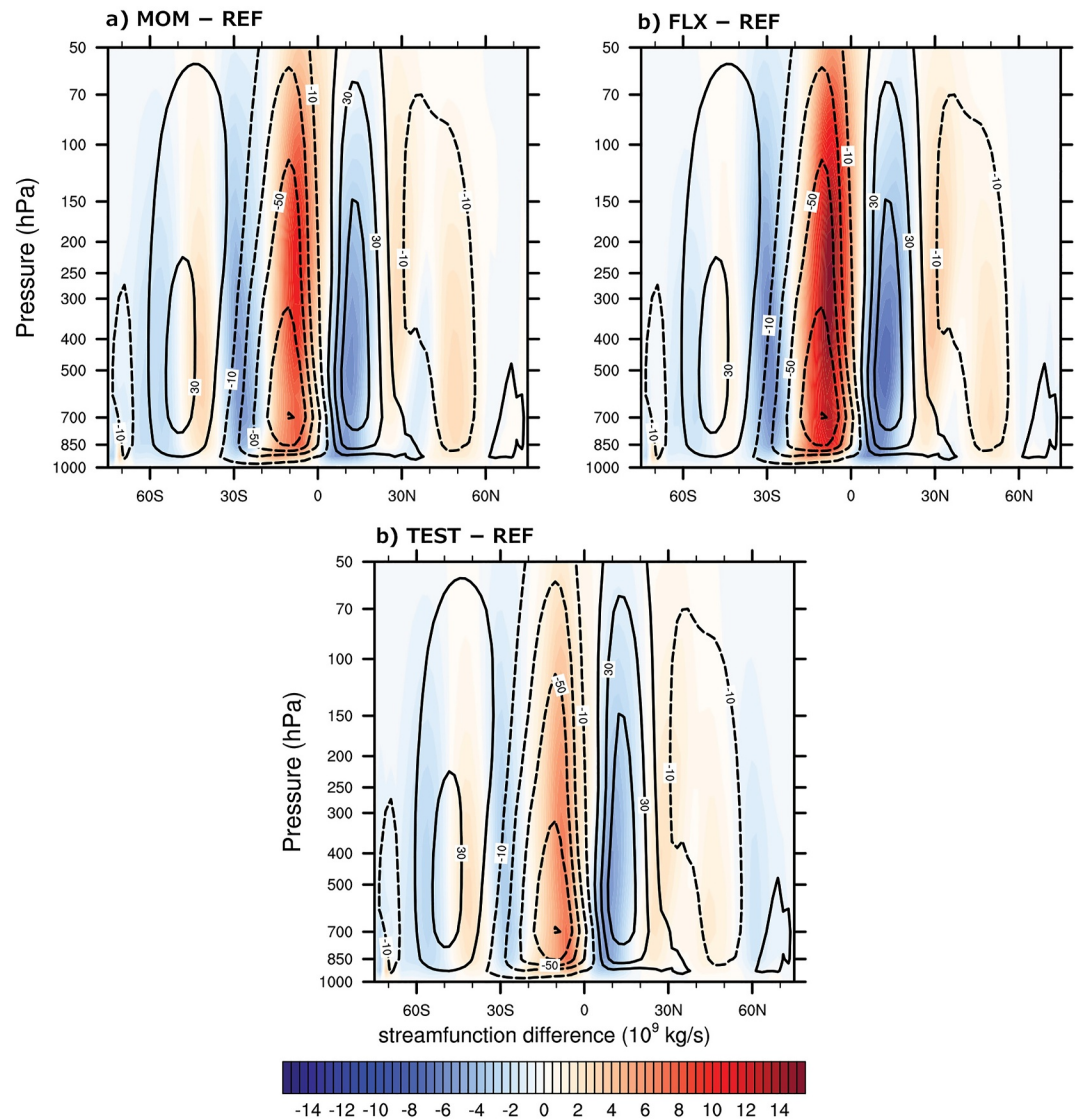


**Figure 6.** Meridional mass streamfunction of the atmospheric circulation. Contours are the streamfunction for the REF simulation, and negative values are indicated with dashed contours. Color shading is the difference between MOM, FLX, or TEST simulation and REF simulation.

The mean meridional circulation is shown in Figure 6, in which the MOM and FLX show significant changes in the strength of the Hadley circulation. The weakening of the Hadley cells is consistent with the weakening of the lower-troposphere trade winds due to the new flux parameterization (Figure 5), and it is probably caused by the weakened meridional winds as a result of the enhanced surface drag. The TEST simulation exhibits qualitatively similar results, whose smaller magnitudes of change can be due to the slightly weaker drag enhancement in TEST (Figure 2). The FLX simulation exhibits a more substantial decrease in the Hadley circulation's strength than the MOM simulation. This difference is intriguing because MOM and FLX share similar levels of enhanced surface drag (Figure 2). A plausible explanation is that the FLX simulation has introduced warming effects through radiation in subtropical latitudes compared with the REF simulation (cf. Section 4.2), thereby reducing meridional temperature gradients in low latitudes. Compared with ERA5 reanalysis, the changes introduced in the new simulations are minimal and do not bring substantial improvement on CESM2's bias regarding the meridional circulation (Figure S5 in Supporting Information S1).

The last aspect of the general circulation we want to examine is the stationary wave patterns, which are critical in determining the zonal asymmetry of the climate (Kaspi & Schneider, 2011). Figure 7 shows the stationary wave

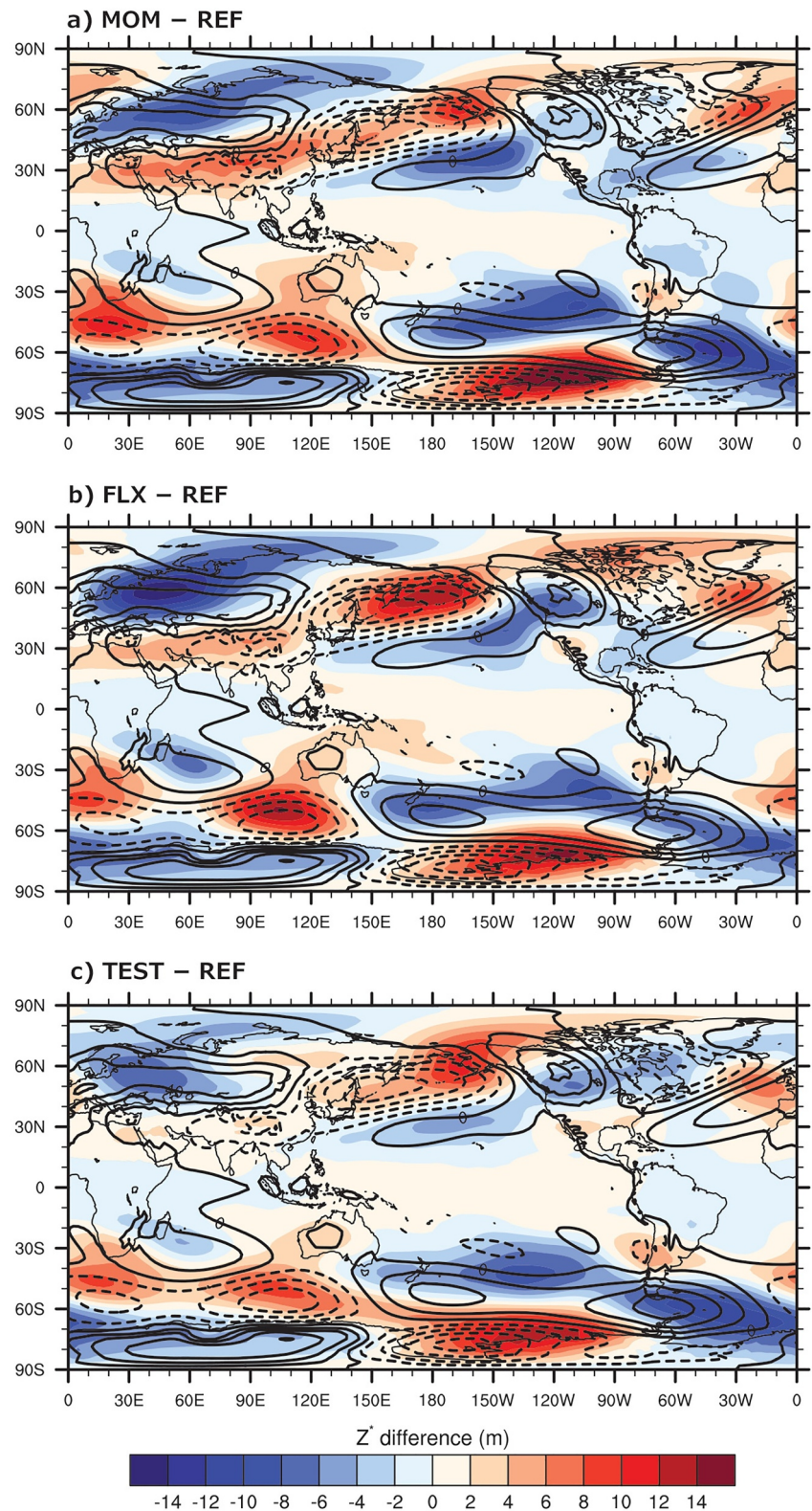


**Figure 7.** Stationary wave component of geopotential height ( $Z^*$ ) at 700 hPa in the simulations.  $Z^*$  is the deviation of time mean geopotential height from the time and zonal mean values. Contours are the  $Z^*$  values of the REF simulation, and color shading is the difference between the MOM, FLX, or TEST and REF simulations. Negative values are indicated with dashed contours.

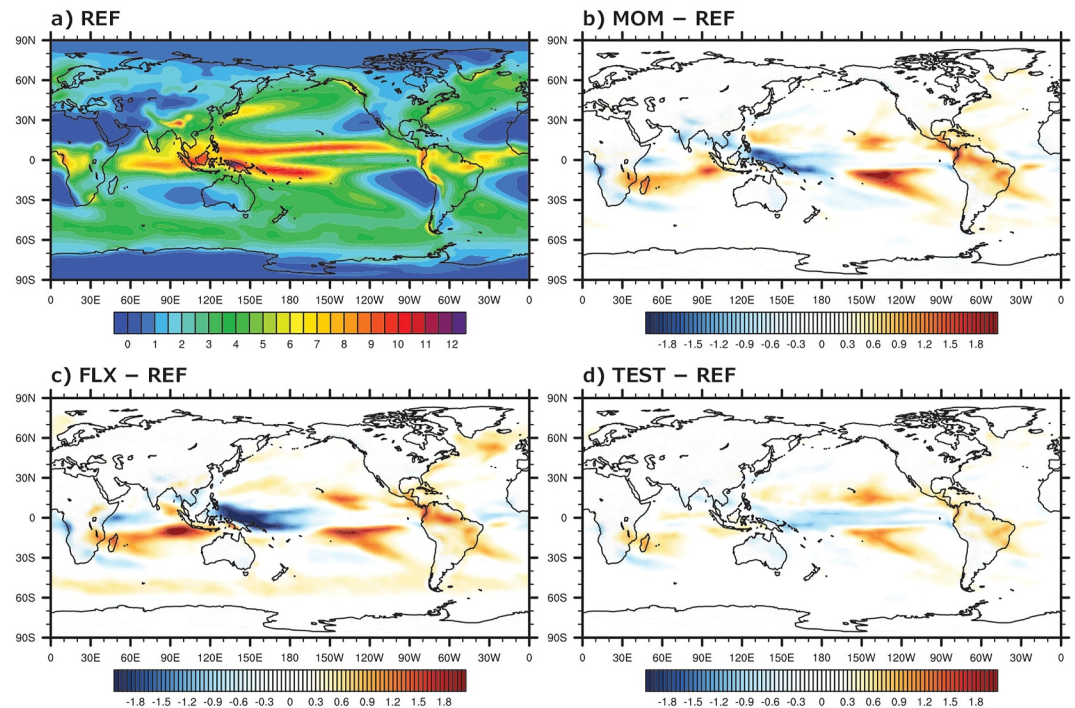


**Figure 8.** Time mean precipitation in the REF simulation (a), the difference in mean precipitation between MOM, FLX, or TEST and REF simulations. The unit is mm/day.

component of the 700-hPa geopotential height field ( $Z^*$ ) and the differences caused by the new parameterizations in MOM and FLX. The climatology of the stationary waves in the REF simulation exhibits anticyclonic circulation in the western part of continents and cyclonic circulation in the eastern side around the coasts in the Northern Hemisphere. Such patterns cause the extra-cold winters in Northeastern North America and Northeastern Asia. By introducing the sea-state-dependent flux parameterizations, the MOM and FLX simulations exhibit weakening of those stationary wave patterns in the extratropics of both the Northern and Southern Hemispheres. This weakening is likely due to the weakening of midlatitude barotropic westerly jets but can also be affected by the corresponding change in baroclinic eddies. The FLX simulation exhibits a more pronounced weakening of the positive  $Z^*$  anomalies in Europe and Western North America, which presumably result from the effects of enhanced latent heat flux on extratropical eddies. The TEST simulation exhibits qualitatively similar patterns of changes, with smaller amplitudes.

#### 4.2. Precipitation, Temperature, and Sea Ice

The effects of the new parameterization on global precipitation are most evident in the tropics and subtropical regions (Figure 8). Compared with the REF simulation, the MOM run exhibits decreased precipitation around the equator, with a larger reduction to the east of the maritime continent. On the other hand, the subtropical region exhibits increases in precipitation, especially in the eastern central Pacific and Indian Ocean and over the Amazon. These changes are consistent with the difference in the Hadley circulation we found above. The weakening of the Hadley circulation reduces rainfall in the deep tropics and allows more convection in the subtropics. The change in the eastern central Pacific and the Amazon suggests the Walker circulation also has a response to the changed surface momentum flux, probably a result of the Hadley circulation variation. Such responses of the subtropical rainfall associated with the Hadley circulation shift are further intensified in the FLX simulation. Rainfall is notably intensified over the Southern Indian Ocean, probably due to the increase in surface latent flux to the south of it (Figure 4), which enhances equatorward moisture transport. Compared with precipitation data of the Global Precipitation Climatology Project analysis (Adler et al., 2018), the MOM and FLX simulations exhibit reduced bias in the Indian Ocean and near the Maritime Continent, but the substantial CESM2 bias near the northern and southern edges of the Pacific ITCZ persists (Figure S6 in Supporting Information S1).

The TEST simulation's response to surface drag enhancement exhibits a similar change in the Hadley circulation, but lacks zonal asymmetry. The precipitation in both the western and eastern Pacific shows decreases compared with the REF simulation. This lack of zonal asymmetry is probably because wave height and age have significant zonal asymmetry in the tropics (Figure 3) but the surface drag adjustment in TEST is zonally uniform.

Surface temperature change due to the new surface flux parameterization is shown in Figure 9. In the MOM simulation, the temperature in the eastern subtropical Pacific Ocean exhibits warming compared with the REF simulation. This warming in the subtropics is likely partially a result of the change in the Hadley circulation, which caused increases in convection in those regions as suggested by the precipitation change (Figure 8). The convective clouds produce radiative forcing and change the atmospheric temperature. Comparing the MOM and REF simulations in Figure 10, we can find that the longwave radiation at the model top has a consistent pattern that exhibits warming effects over the eastern subtropical Pacific. Meanwhile, the poleward heat transport by the subtropical ocean gyres exhibits significant increases, which also contribute to the warming in the subtropical ocean (cf., Section 4.3). The temperature near the west coast of South America and Africa exhibits some cooling, probably due to the enhanced surface drag that strengthens upwelling near the coast. This cooling is additionally enhanced due to low-cloud feedback, which is evidenced by the model top radiation change (Figure 10). Additionally, the change in surface drag might change the mixed layer depth through modulating the “wind work,” therefore impacting temperature in some regions (Luongo et al., 2024).

The FLX simulation exhibits a similar pattern of changes. However, the warming in the Northern Hemisphere subtropical Pacific becomes weaker and shifts westward. The cooling along the west coast of continents extends to North America as well. More pronounced differences between the MOM and FLX simulations include the enhanced warming over the northern Eurasia continent and the significant cooling in the Southern Ocean near the Antarctica coast. The warming over the Eurasia continent is likely a result of the change in stationary wave patterns, the weakening of which reduces the zonal asymmetry of midlatitude climate. North America's temperature also exhibits similar differences between MOM and FLX, though the magnitude of the difference is smaller. The strengthening of the Atlantic Meridional Overturning Circulation (AMOC) in FLX, discussed in the next section, may also contribute to the warming over the Eurasia continent in FLX. The cooling in the Southern Ocean happens in tandem with seasonal sea ice changes, which are discussed below when we document the sea ice responses. The TEST simulation exhibits a pattern similar to the MOM simulation but with slightly weaker changes.

Figure S7 in Supporting Information S1 shows the global mean, global sea-surface mean, and global land-surface mean temperature in the 40 years of the simulations. The time series of ERA5 reanalysis surface temperature is also included for comparison. The CESM2 simulations show a warm bias over both land and oceans. The new parameterizations do not cause a significant change in global mean land surface temperature. However, the global mean SST bias is reduced over oceans from about 0.6 to 0.3°. Meanwhile, the oceans' inter-decadal variability in the FLX simulation seems excessively large compared with that in ERA5 data.

Another interesting finding about the new surface flux schemes is that sea ice near the Antarctic coast is very sensitive to changes in surface stress and fluxes. Figure 11a shows the observed climatological mean sea ice area fraction in the Antarctic region, and Figure 11b shows the bias in the default REF simulation. Figures 11c and 11d are the bias of MOM and FLX simulations with the new sea-state dependent surface flux parameterizations. Their difference with the REF simulation is shown in Figure S8 in Supporting Information S1. In MOM, where wind stress is modified, the time mean ice fraction increases in the Weddell Sea and reduces local bias compared with the observation. It has been suggested that wind-driven ice advection is an essential mechanism in governing the ice concentration around West Antarctica, and strengthened westerly winds are responsible for sea ice loss in some years (Holland & Kwok, 2012; Turner et al., 2020). Thus, the increase in sea ice in the Weddell Sea in our MOM simulations directly results from the enhanced drag coefficient and the weakened westerlies in the lower troposphere. The TEST simulation exhibits a response pattern similar to the MOM simulation, with weaker magnitudes of changes.

In contrast, the FLX simulation exhibits increased sea ice cover around Antarctica for all longitudes. The bias in the Southern Ocean in the sector between 30°W and 60°E is further reduced, but the positive bias between 60°E and 150°E increases. The difference between the FLX and MOM simulations is the decreased sensible heat and increased latent heat flux. The former can directly reduce near-surface air temperature. The latter can enhance clouds, especially those at low levels. We evaluated the net radiative flux at the model top (Figure 10) and found

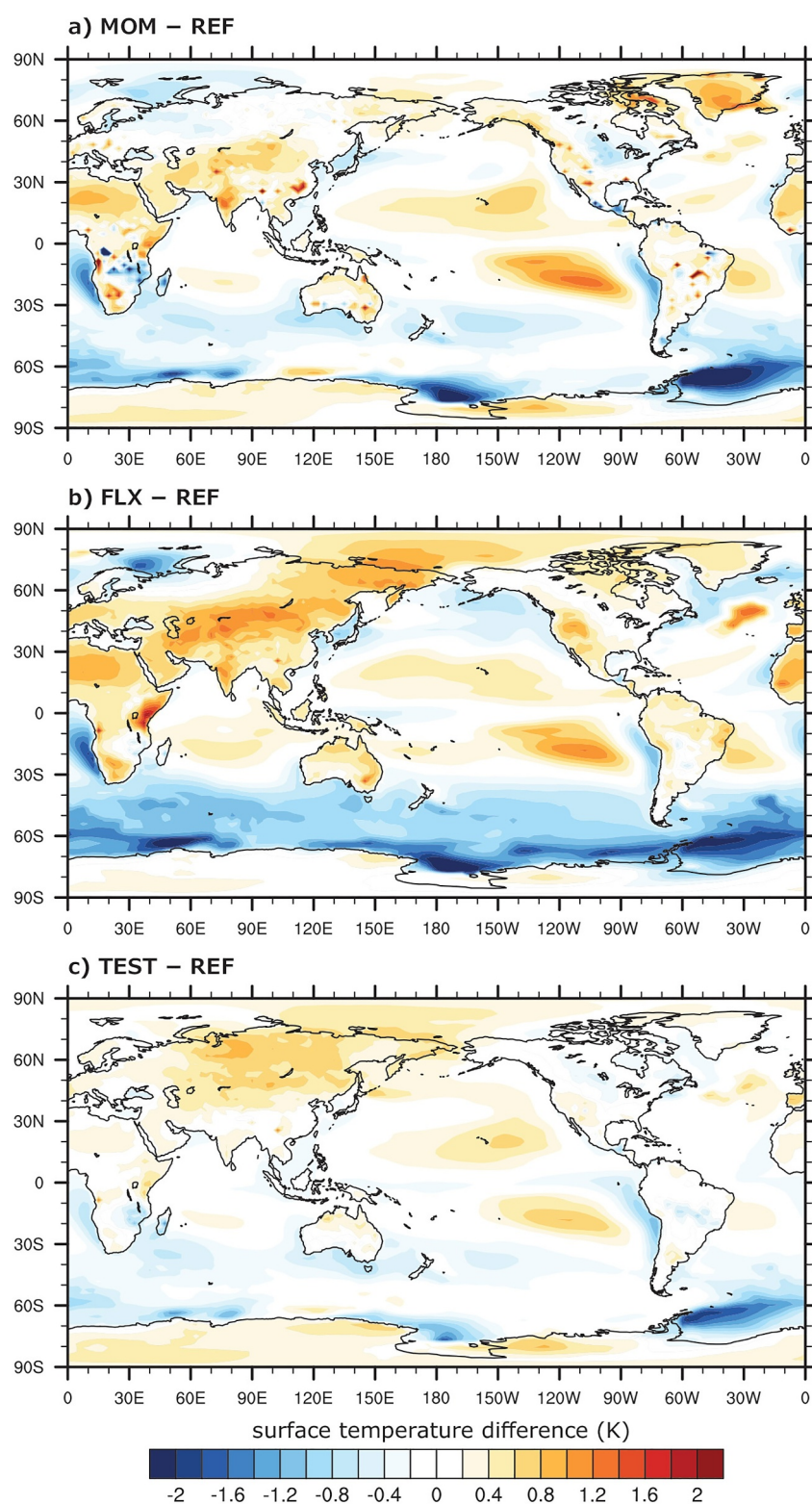


**Figure 9.** Time mean surface temperature difference between MOM, FLX, or TEST and REF simulations.

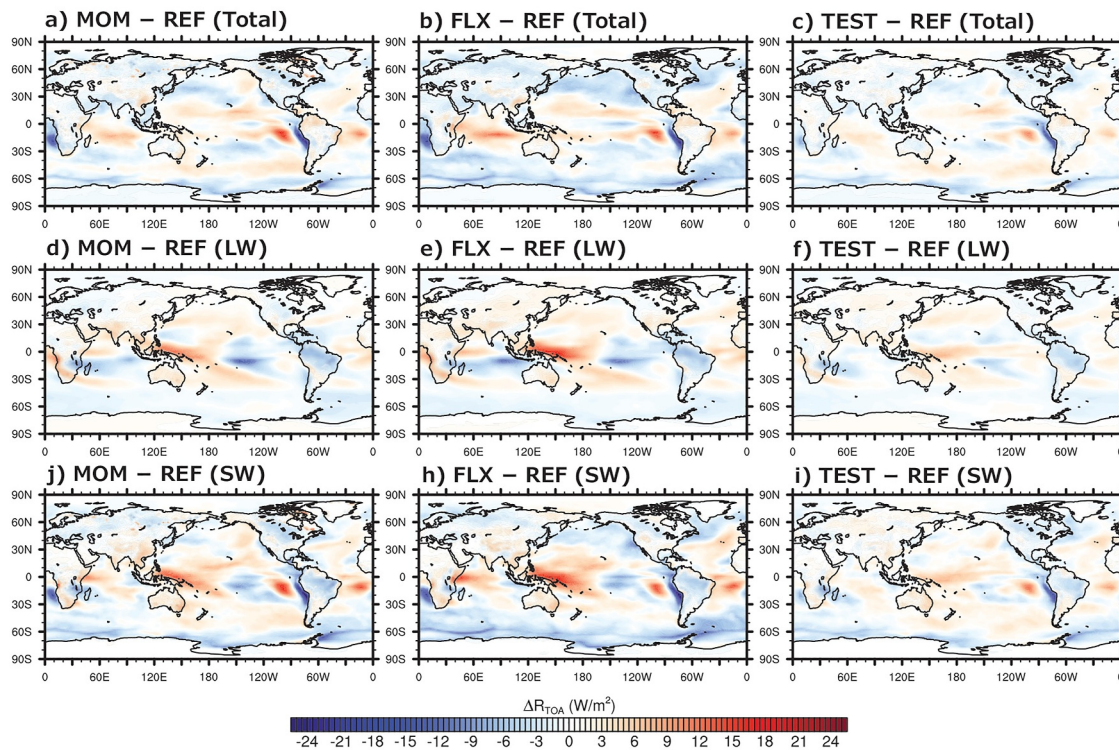


**Figure 10.** Time mean net radiation flux differences at the model top between MOM, FLX, or TEST and REF simulations. Panels (a–c) are for the net total radiative flux (shortwave + longwave); (d–f) for the net longwave radiation; (j), (h), and (i) are for the net shortwave radiation. The positive direction for total and shortwave is downward, and the positive direction for longwave is upward.

that FLX exhibits decreases in the shortwave flux at mid- and high-latitudes in the Southern Hemisphere, whereas the MOM or TEST simulation does not share similar decreases in shortwave flux. This implies a change in planetary albedo due to low clouds.

It should be noted that once sea ice forms and expands northward, it can cut off sensible flux from the relatively warm water, thereby further lowering near-surface air temperature and enhancing sea ice expansion. Therefore, the increases of sea ice in FLX compared with MOM and REF likely involve the interaction between surface flux, cloud, and sea ice. The temperature decrease pattern (Figure 9) around the Antarctica does not resemble the pattern of sensible or latent heat flux changes (Figure 4). Thus, the increases in sea ice appear to play a more direct role in the substantial decreases in the SST in the Southern Ocean, which yield favorable improvement to reduce the ocean surface temperature bias in the simulations. The Arctic region does not share similar increases due to the new surface flux parameterization. Actually, it exhibits slight decreases (<5%) in the sea ice fraction in the Asian-side Arctic region, probably due to the corresponding temperature change.

### 4.3. Ocean Meridional Overturning Circulation

The global meridional overturning circulation (MOC) in the simulations is shown in Figure 12. The dominant features are the AMOC and the Southern Meridional Overturning Circulation (SMOC). Introducing the wave-dependent wind stress in the MOM simulation does not affect the AMOC much. However, the SMOC's subsiding branch related to the Antarctic Intermediate Water is enhanced, and its upwelling branch related to the Circumpolar Deep Water is weakened. This northward shift of SMOC may be primarily due to the wind stress change but could be affected to some extent by the sea ice change.

In contrast, the FLX simulation significantly strengthens the subsiding branch of the AMOC. Figure 4 shows that near the surface, latent heat flux is substantially enhanced to the south of Greenland, where wave height is large due to wave dynamics (Figure 3). The response in the AMOC is likely due to the cooling and increase in salinity

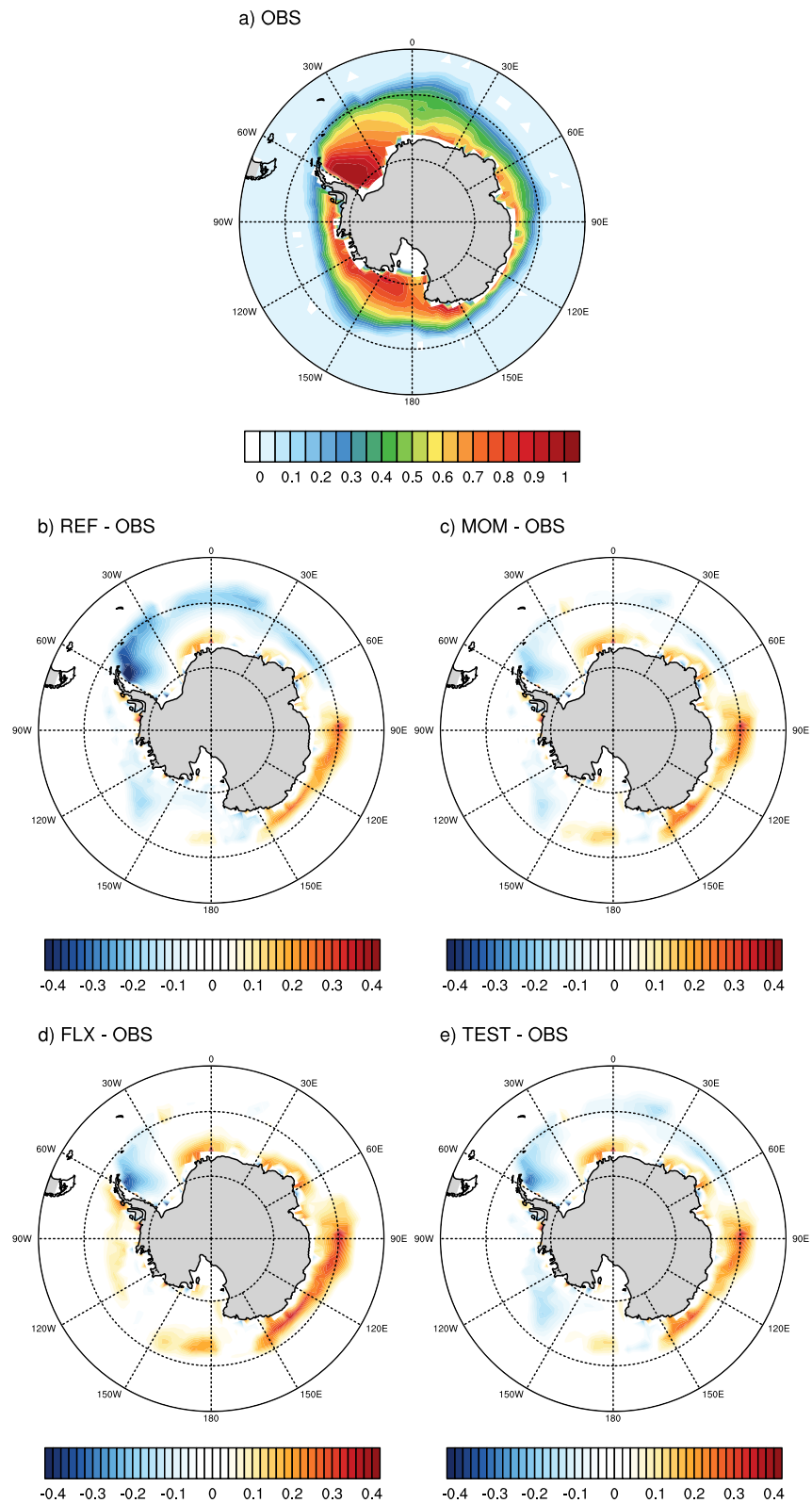


**Figure 11.** Time mean of the surface area fraction covered by sea ice in observation (a) and the differences between REF, MOM, FLX, or TEST and observation (b–e). The observation is the Sea Ice Concentration Climate Data Record, version 3 (OSI SAF, 2022).

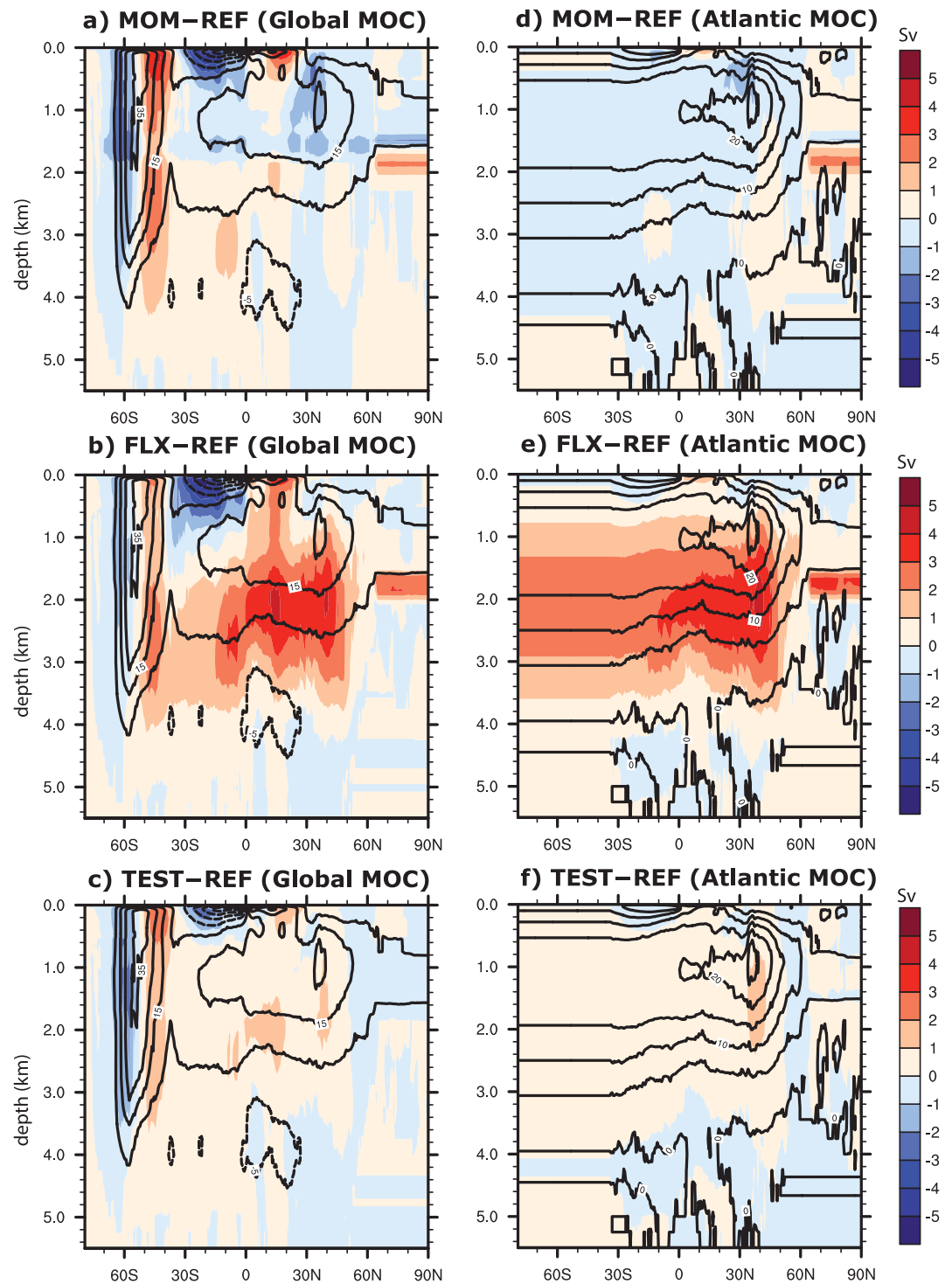


**Figure 12.** Ocean meridional overturning circulation for the globe (a–c) and Atlantic (d–f). Contours show the streamfunction of the REF simulation, and color shading is the difference between MOM, FLX, or TEST simulations and the REF simulation.

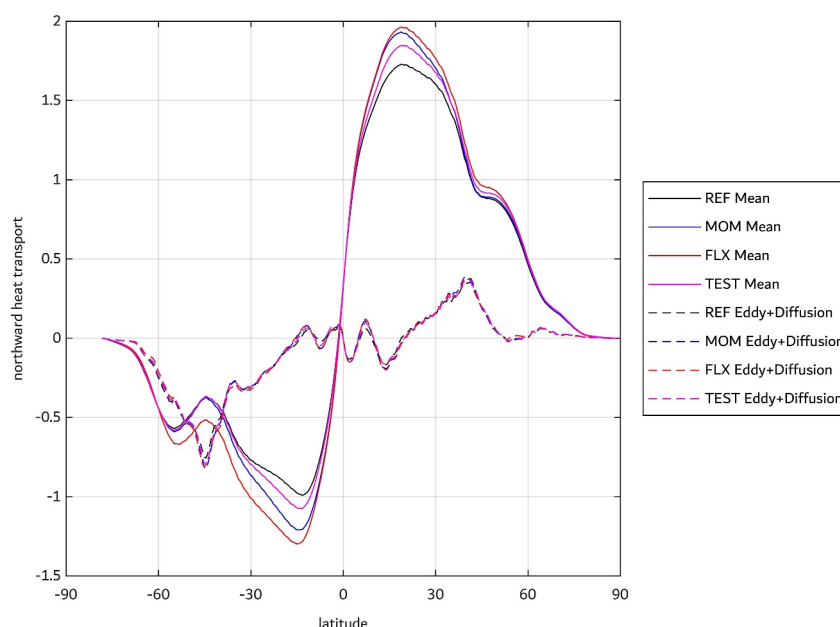


**Figure 13.** Global meridional heat transport by the oceans. Solid lines show the time mean total meridional heat flux of different simulations, and dashed lines show the contribution from eddies and diffusion.

of the near-surface water (Figure S9 in Supporting Information S1) in the North Atlantic, as the latent heat flux is enhanced in FLX.

The meridional heat transport by the ocean circulation is shown in Figure 13. The largest changes in amplitudes are in subtropical regions. MOM and FLX exhibit increasingly stronger poleward heat transport peaking around 15°N/S. Their peaks are about 18% higher than that in the REF simulation. The heat transport at those latitudes is generated by the shallow overturning circulations associated with subtropical gyres, which are driven by atmospheric winds. Approximately between 40° and 50° in the Southern and Northern Hemispheres, the differences between MOM and REF is small, but their poleward heat fluxes are weaker than that of the FLX simulation by about 20%. Those differences are due to changes in the deeper thermohaline circulations. The enhancement of AMOC probably contributed to the Eurasia continent warming in FLX compared with MOM and REF. The changes in meridional heat transport are mainly caused by changes in the Eulerian mean circulation in the ocean, the eddies' contribution is minimal. The TEST simulation exhibits some effects on enhancing the subtropical region meridional heat transport but has no effect on the flux around 50°S.

#### 4.4. Global Warming Trend

Lastly, we evaluate how the new surface flux schemes impact anthropogenic temperature change. Figure 14 shows the surface temperature change from the first 10-year period (1975–1984) to the last 10-year period (2005–2014) in our simulations and the ERA5 reanalysis. A notable bias of climate change in the REF simulation is the warming in northern Asia, which is too strong compared with the reanalysis. MOM and FLX simulations reduced the warming bias in the north of Asia continent.

Another substantial improvement is in the Pacific, where coupled climate models in CMIP6 persistently exhibit warming in recent decades while observation indicates slight cooling (Seager et al., 2022; Wills et al., 2022). The MOM simulation can produce some cooling over the recent decades in the Southern Hemisphere and tropical and subtropical Pacific, but still has a warming bias in the Northern Hemisphere Pacific near the west coast of North America.

Interestingly, the FLX simulation can reproduce the rough cooling pattern in the eastern Pacific in both hemispheres and tropical regions. However, the cooling in the Southern Ocean and near the equator is not at the exact locations shown in the reanalysis. Off the coast of northern Japan, FLX suffers from a warming bias. Those issues might be related to the coarse resolutions of all components in our simulations, especially the WW3 module.

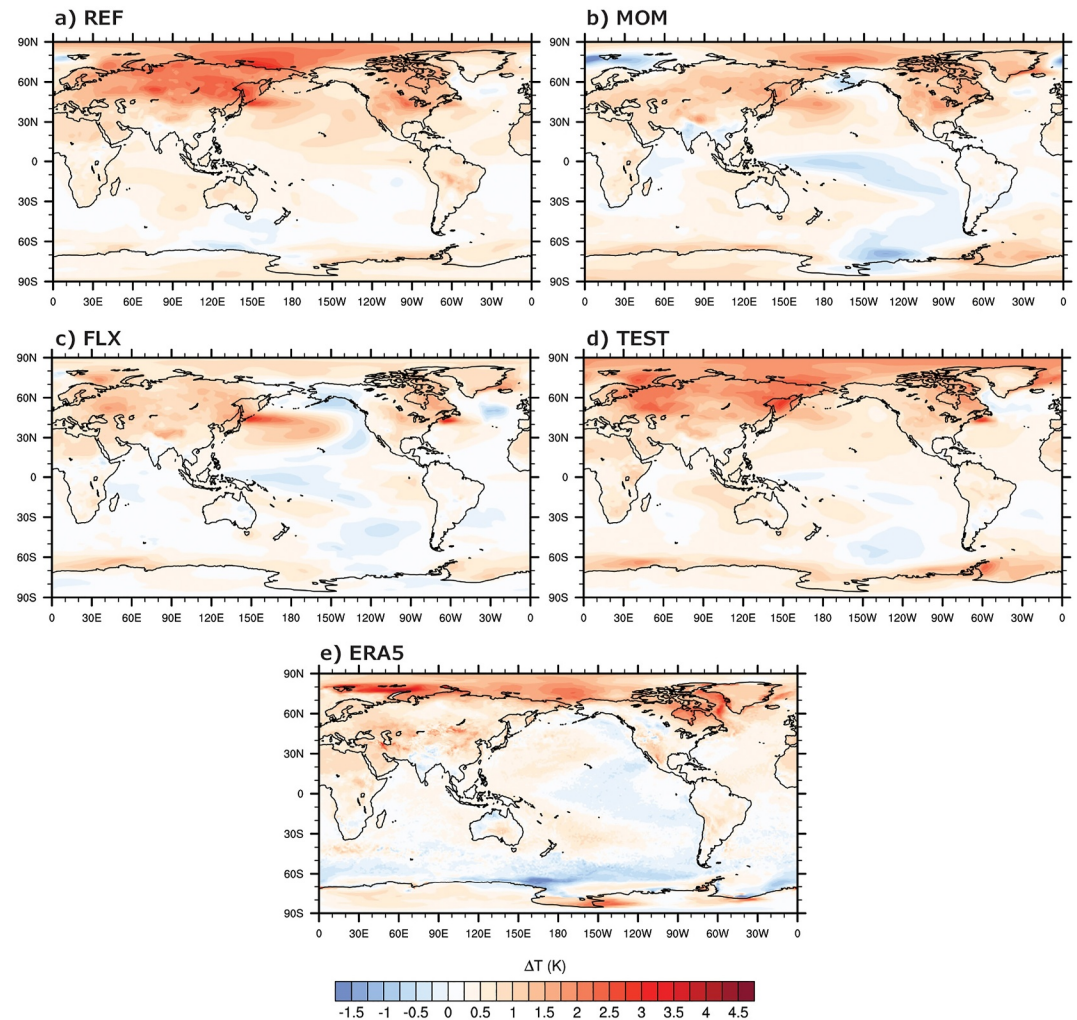


**Figure 14.** Temperature difference between the time average of the last 10 years (2005–2014) and first 10 years (1975–1984) of the four CESM2 simulations and the ERA5 reanalysis.

However, it should be noted that the Extended Reconstructed SST data set v5 (ERSSTv5) (Huang et al., 2017) indeed exhibits some relatively strong warming trend to the east of Japan, which is mild in ERA5 reanalysis (Wills et al., 2022).

It should be noted that the wave characteristics also undergo some changes under global warming. Figure 15 shows the difference between the last 10 years and the first 10 years mean. While the phase speed field does not change significantly in most places, the wave height field exhibits increases in the Southern Ocean and decreases in the North Pacific and North Atlantic. Those changes are roughly consistent with previous studies (Fan et al., 2013; Reguero et al., 2019). These changes might feed back to other components of the climate system. The trends of surface wind stress exhibit notable differences between the REF and FLX simulations (Figure S10 in Supporting Information S1). In the Southern Ocean, wind stress increases in some regions and decreases in others in the REF simulation. In contrast, in the FLX simulation, an increasing trend prevails throughout the Southern Ocean. In the North Pacific Ocean, the REF simulation exhibits decreases in wind stress in most places except in its middle part off the west coast of the United States. However, the FLX simulation exhibits a significant decreasing trend in mid-latitude North Pacific and a weak enhancement of wind stress in the Northern and subtropical part of the North Pacific Ocean. While the wave height changes are likely a result of changing wind conditions, their feedback can alter the patterns of wind stress changes in FLX, which, in turn, might have contributed to the weak cooling trend in some parts of the ocean in Figure 14 by modulating ocean gyres. This

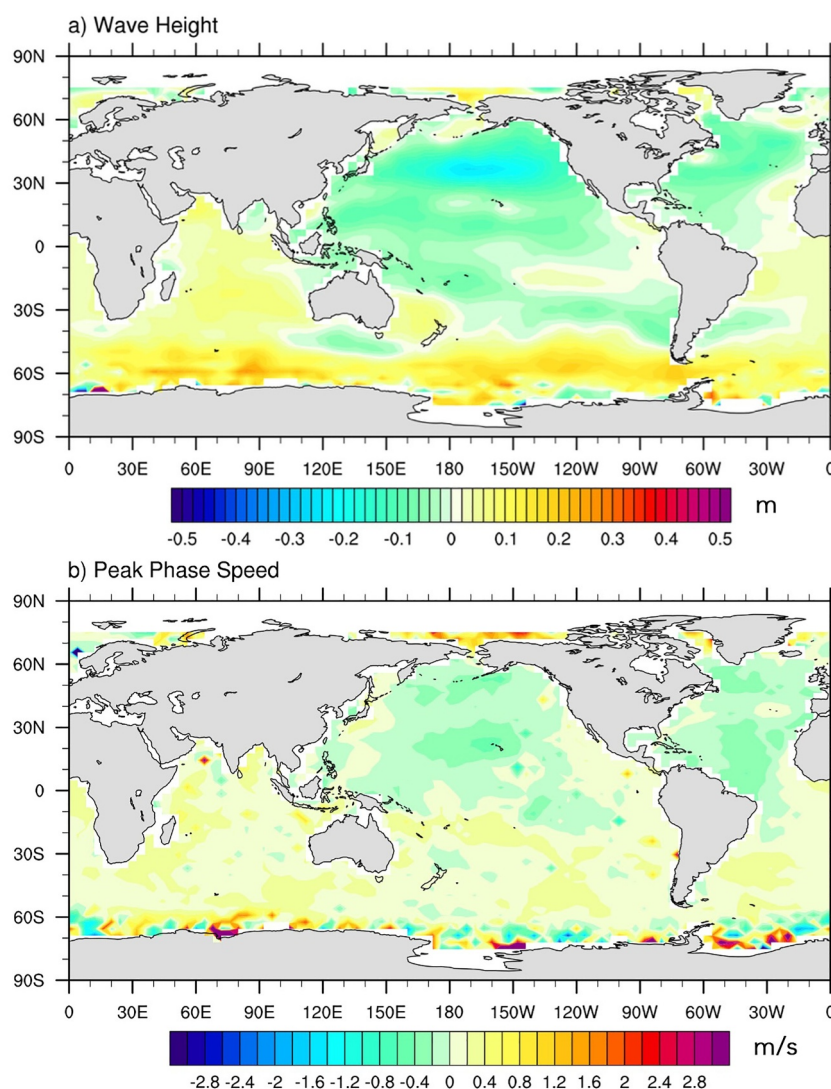


**Figure 15.** Differences of wave height (a) and peak phase speed (b) between the time average of the last 10 years (2005–2014) and the first 10 years (1975–1984) of the FLX simulation.

hypothesis needs more detailed analysis in higher-resolution, large ensemble simulation settings; we will address it in future work.

## 5. Summary and Discussion

By analyzing the wind biases in climate simulations compared with reanalysis, Simpson et al. (2018) suggest that there might be a missing process in climate models that constitutes a missing drag on the low-level zonal flow over oceans. Conventional air-sea flux parameterizations estimate fluxes from near-surface atmospheric stability and air-sea differences in velocity, temperature, and water vapor. However, the presence of ocean surface gravity waves introduces additional variability that cannot be described by atmospheric stability or air-sea differences.

In this study, we implemented a sea-state-dependent surface flux parameterization in CESM2 and evaluated its impact on the mean climate states and historical trends. Surface momentum flux is modified through wave-dependent roughness lengths, and sensible and latent heat fluxes are modified through the new roughness formula and considering the effects of sea spray. The surface drag coefficient for momentum increases at all latitudes in the simulations with the new parameterization, but surface wind stress shows decreases at some latitudes, such as over the Southern Ocean and the central Pacific near the equator. Those changes in surface wind stress, on the

one hand, depend on the regional characteristics of waves and, on the other hand, depend on the mean state change in the atmospheric circulation. Sea-spray dependency, in general, decreases surface sensible heat flux and increases latent heat flux. The latter dominates and exhibits significant changes in mid- and high-latitude oceans.

The new wave-dependent schemes bring noticeable changes in the mean climate states into the simulations in CESM2. High bias in the Southern Hemisphere barotropic jet is reduced, especially in the lower and middle troposphere. Hadley Circulation is weakened due to the new schemes, causing decreases in the precipitation in the deep tropics to the east of the maritime continents and increases in the eastern subtropical Pacific. Extratropical stationary wave patterns are weakened, leading to a more zonally symmetric climate. Notable differences in surface temperature are exhibited with those circulation changes, especially in the FLX simulation, which includes both the new momentum and enthalpy flux schemes. Compared with the REF simulation without those new schemes, the FLX simulation exhibits warmer temperatures over the northern Asia continent and a significantly cooler Southern Ocean. The temperature change in the Southern Ocean is related to the expansion of sea ice around Antarctica, which is likely a result of the effects of enhanced surface latent heat flux on low clouds.

The new surface flux schemes also have an important impact on the ocean. The slight cooling in the eastern Pacific in recent decades is missing in the reference run, but it is partially produced in the FLX simulation with both the new momentum and enthalpy flux parameterizations. The new schemes also substantially enhance the mean strength of the AMOC, likely through cooling and increasing the salinity of upper-level water in the North Atlantic by enhancing evaporation.

The TEST simulation, in which surface drag is artificially amplified, provided a baseline understanding of the new simulations' effects while evaluating the robustness of the simulation results. The change in the zonal mean wind in the lower and middle troposphere can be reproduced in the TEST simulation, suggesting that those changes in MOM and FLX are primarily due to enhanced surface drag. However, tropical precipitation changes differ in those simulations because surface wave characteristics have zonal asymmetry, and their effect on tropical circulation cannot be modeled as a simple enhancement of surface drag. Other changes in sea ice and the AMOC depend on the change in surface sensible and latent heat flux, and therefore, they cannot be reproduced in the TEST simulation. The long-term SST trends also differ in MOM, FLX, and TEST simulations. It is difficult to conclude to what extent those differences are due to parameterization details and to what extent they result from natural variability. To address this issue, large ensemble simulations are needed to disentangle natural variability and model differences.

Our simulations still have notable biases in various metrics, such as the global mean land surface temperature. Those biases might be due to the coarse resolutions we used in the atmosphere and wave components of the CESM2 simulations. The low resolution might under-resolve details of atmospheric and ocean dynamics. In general, running WW3 in long climate simulations is computationally expensive. The coarse resolution for WW3 in CESM therefore represents a compromise trying to balance model accuracy and computational cost. The authors' previous experience with WW3 suggests that coarsening the spectral resolution in WW3 leads to greater error in wave statistics than coarsening the spatial resolution (Q. Li et al., 2016). Since we are focusing on the effects of sea-state-dependent surface fluxes on the mean climate state, we don't expect that the main conclusions in the work will change significantly with WW3 running on a higher resolution. Higher resolution for WW3 may be required to capture the variability of the wave states induced by extreme winds (such as during a hurricane) and their contribution to wind stress (e.g., Reichl et al., 2014), which also requires higher resolution for the atmosphere model. This is computationally expensive for long climate simulations as those in this study and is left for future research. The high computational cost of wave coupling in long climate simulations has motivated alternative approaches to represent the effects of waves (e.g., Q. Li et al., 2017; Hell et al., 2024).

In addition, parameterization schemes are likely tuned for the default CESM2 resolutions. Therefore, they probably produce biases when the model is run at coarse resolutions. Even at standard resolutions, adding a new parameterization to some extent requires tuning other parameterizations in CESM2, which we did not do and may have produced some compensating errors in the simulations. Our simulations are also relatively short and, therefore, likely contaminated by low-frequency variability. While we seek a physically reasonable understanding of the impact of the new surface flux parameterizations, the complex feedback in a fully coupled Earth system model means that the improvements and remaining biases may result from coupled dynamics rather than being caused by a single process.

Lastly, the wave age in the deep tropics and the wave height in the Southern Ocean typically fall outside the observation data range (Table S1 in Supporting Information S1) used to develop the scheme of Lin et al. (2021). While we do not expect fundamental changes in the physical relations, it would be valuable to have more observational data sets of sea state and surface fluxes in those regions to further constrain and refine sea-state-dependent flux parameterizations, given that those two regions play critical roles in influencing the climate system dynamics through processes discussed in this study. Nevertheless, our experiments demonstrate that including sea-state dependency in surface flux parameterizations has excellent potential to elevate the fidelity of Earth system simulations. More investigation with refined model resolutions and carefully tuned parameters is warranted in future studies.

## Conflict of Interest

The authors declare no conflicts of interest relevant to this study.

## Data Availability Statement

The modified CESM2 code, incorporating wave-dependent surface flux parameterizations, involves several components: CIME, WW3, and CAM, which are publicly available at <https://github.com/MetLab-HKUST/Flux-CIME>, <https://github.com/MetLab-HKUST/Flux-CAM>, and <https://github.com/MetLab-HKUST/Flux-WW3>. They are archived on Zenodo (Shi, 2025b). The data and analysis scripts for the figures in this study are archived in Shi (2025a).

## Acknowledgments

We thank Dr. Brandon Reichl and the other two anonymous reviewers for their valuable suggestions, which significantly improved our manuscript. The work described in this paper was substantially supported by a grant from the Research Grants Council (RGC) of the Hong Kong Special Administrative Region, China (Project Reference Number: AoE/P-601/23-N) and the Center for Ocean Research in Hong Kong, and Macau (CORE), a joint research center between the Laoshan Laboratory and the Hong Kong University of Science and Technology (HKUST). XS is additionally supported by the RGC Grant HKUST-16301322, and QL is additionally supported by the National Natural Science Foundation of China (42206031). The authors thank HKUST Fok Ying Tung Research Institute and the National Supercomputing Center in Guangzhou Nansha sub-center for providing high-performance computational resources.

## References

- Adler, R. F., Sapiiano, M. R., Huffman, G. J., Wang, J.-J., Gu, G., Bolvin, D., et al. (2018). The global precipitation climatology project (GPCP) monthly analysis (new version 2.3) and a review of 2017 global precipitation. *Atmosphere*, 9(4), 138. <https://doi.org/10.3390/atmos9040138>
- Andreas, E. L. (1989). *Thermal and size evolution of sea spray droplets. CRREL report 89-11 (NTIS ADA210484)*. US Army Cold Regions Research and Engineering Laboratory.
- Andreas, E. L. (1990). Time constants for the evolution of sea spray droplets. *Tellus B: Chemical and Physical Meteorology*, 42(5), 481–497. <https://doi.org/10.3402/tellusb.v42i5.15241>
- Andreas, E. L. (1992). Sea spray and the turbulent air-sea heat fluxes. *Journal of Geophysical Research*, 97(C7), 11429–11441. <https://doi.org/10.1029/92jc00876>
- Andreas, E. L. (1995). The temperature of evaporating sea spray droplets. *Journal of the Atmospheric Sciences*, 52(7), 852–862. [https://doi.org/10.1175/1520-0469\(1995\)052<0852:ttoess>2.0.co;2](https://doi.org/10.1175/1520-0469(1995)052<0852:ttoess>2.0.co;2)
- Andreas, E. L. (1998). A new sea spray generation function for wind speeds up to 32 m s<sup>-1</sup>. *Journal of Physical Oceanography*, 28(11), 2175–2184. [https://doi.org/10.1175/1520-0485\(1998\)028<2175:anssgf>2.0.co;2](https://doi.org/10.1175/1520-0485(1998)028<2175:anssgf>2.0.co;2)
- Andreas, E. L., Mahrt, L., & Vickers, D. (2015). An improved bulk air-sea surface flux algorithm, including spray-mediated transfer. *Quarterly Journal of the Royal Meteorological Society*, 141(687), 642–654. <https://doi.org/10.1002/qj.2424>
- Andreas, E. L., Persson, P. O. G., & Hare, J. E. (2008). A bulk turbulent air-sea flux algorithm for high-wind, spray conditions. *Journal of Physical Oceanography*, 38(7), 1581–1596. <https://doi.org/10.1175/2007jpo3813.1>
- Bao, Y., Song, Z., & Qiao, F. (2020). Fio-esm version 2.0: Model description and evaluation. *Journal of Geophysical Research: Oceans*, 125(6), e2019JC016036. <https://doi.org/10.1029/2019jc016036>
- Barnes, E. A., & Garfinkel, C. I. (2012). Barotropic impacts of surface friction on eddy kinetic energy and momentum fluxes: An alternative to the barotropic governor. *Journal of the Atmospheric Sciences*, 69(10), 3028–3039. <https://doi.org/10.1175/jas-d-11-0243.1>
- Barsugli, J. J., & Battisti, D. S. (1998). The basic effects of atmosphere-ocean thermal coupling on midlatitude variability. *Journal of the Atmospheric Sciences*, 55(4), 477–493. [https://doi.org/10.1175/1520-0469\(1998\)055<0477:tbeoao>2.0.co;2](https://doi.org/10.1175/1520-0469(1998)055<0477:tbeoao>2.0.co;2)
- Bernardet, L., Tallapragada, V., Bao, S., Trahan, S., Kwon, Y., Liu, Q., et al. (2015). Community support and transition of research to operations for the hurricane weather research and forecasting model. *Bulletin of the American Meteorological Society*, 96(6), 953–960. <https://doi.org/10.1175/bams-d-13-00093.1>
- Cavaleri, L., Fox-Kemper, B., & Hemer, M. (2012). Wind waves in the coupled climate system. *Bulletin of the American Meteorological Society*, 93(11), 1651–1661. <https://doi.org/10.1175/bams-d-11-00170.1>
- Chen, G., Chapron, B., Ezraty, R., & Vandemark, D. (2002). A global view of swell and wind sea climate in the ocean by satellite altimeter and scatterometer. *Journal of Atmospheric and Oceanic Technology*, 19(11), 1849–1859. [https://doi.org/10.1175/1520-0426\(2002\)019<1849:agvo>2.0.co;2](https://doi.org/10.1175/1520-0426(2002)019<1849:agvo>2.0.co;2)
- Chen, S. S., Zhao, W., Donelan, M. A., & Tolman, H. L. (2013). Directional wind-wave coupling in fully coupled atmosphere-wave-ocean models: Results from CBLAST-hurricane. *Journal of the Atmospheric Sciences*, 70(10), 3198–3215. <https://doi.org/10.1175/jas-d-12-0157.1>
- Danabasoglu, G., Lamarque, J.-F., Bacmeister, J., Bailey, D., DuVivier, A., Edwards, J., et al. (2020). The community earth system model version 2 (CESM2). *Journal of Advances in Modeling Earth Systems*, 12(2), e2019MS001916. <https://doi.org/10.1029/2019ms001916>
- Davis, C., Wang, W., Chen, S. S., Chen, Y., Corbosiero, K., DeMaria, M., et al. (2008). Prediction of landfalling hurricanes with the advanced hurricane WRF model. *Monthly Weather Review*, 136(6), 1990–2005. <https://doi.org/10.1175/2007mwr2085.1>
- Drennan, W. M., Graber, H. C., Hauser, D., & Quentin, C. (2003). On the wave age dependence of wind stress over pure wind seas. *Journal of Geophysical Research*, 108(C3), 8062. <https://doi.org/10.1029/2000jc000715>
- Drennan, W. M., Taylor, P. K., & Yelland, M. J. (2005). Parameterizing the sea surface roughness. *Journal of Physical Oceanography*, 35(5), 835–848. <https://doi.org/10.1175/jpo2704.1>
- Edson, J. B., Jampana, V., Weller, R. A., Bigorre, S. P., Plueddemann, A. J., Fairall, C. W., et al. (2013). On the exchange of momentum over the open ocean. *Journal of Physical Oceanography*, 43(8), 1589–1610. <https://doi.org/10.1175/jpo-d-12-0173.1>

- Emanuel, K. A. (1986). An air-sea interaction theory for tropical cyclones. Part I: Steady-state maintenance. *Journal of the Atmospheric Sciences*, 43(6), 585–605. [https://doi.org/10.1175/1520-0469\(1986\)043<0585:asaitf>2.0.co;2](https://doi.org/10.1175/1520-0469(1986)043<0585:asaitf>2.0.co;2)
- Fairall, C. W., Bradley, E. F., Hare, J., Grachev, A. A., & Edson, J. B. (2003). Bulk parameterization of air–sea fluxes: Updates and verification for the COARE algorithm. *Journal of Climate*, 16(4), 571–591. [https://doi.org/10.1175/1520-0442\(2003\)016<0571:bpoasf>2.0.co;2](https://doi.org/10.1175/1520-0442(2003)016<0571:bpoasf>2.0.co;2)
- Fan, Y., Held, I. M., Lin, S.-J., & Wang, X. L. (2013). Ocean warming effect on surface gravity wave climate change for the end of the twenty-first century. *Journal of Climate*, 26(16), 6046–6066. <https://doi.org/10.1175/jcli-d-12-00410.1>
- Fischer, E., Beyerle, U., Schleussner, C.-F., King, A. D., & Knutti, R. (2018). Biased estimates of changes in climate extremes from prescribed SST simulations. *Geophysical Research Letters*, 45(16), 8500–8509. <https://doi.org/10.1029/2018gl079176>
- García-Nava, H., Ocampo-Torres, F., Osuna, P., & Donelan, M. (2009). Wind stress in the presence of swell under moderate to strong wind conditions. *Journal of Geophysical Research*, 114(C12), C12008. <https://doi.org/10.1029/2009jc005389>
- Garfinkel, C. I., Oman, L. D., Barnes, E. A., Waugh, D. W., Hurwitz, M. H., & Molod, A. M. (2013). Connections between the spring breakup of the southern hemisphere polar vortex, stationary waves, and air–sea roughness. *Journal of the Atmospheric Sciences*, 70(7), 2137–2151. <https://doi.org/10.1175/jas-d-12-0242.1>
- Hanley, K. E., Belcher, S. E., & Sullivan, P. P. (2010). A global climatology of wind–wave interaction. *Journal of Physical Oceanography*, 40(6), 1263–1282. <https://doi.org/10.1175/2010jpo4377.1>
- He, J., & Soden, B. J. (2016). Does the lack of coupling in SST-forced atmosphere-only models limit their usefulness for climate change studies? *Journal of Climate*, 29(12), 4317–4325. <https://doi.org/10.1175/jcli-d-14-00597.1>
- Hell, M., Chapron, B., & Fox-Kemper, B. (2024). A particle-in-cell wave model for efficient sea-state and swell estimates in earth system models-picles. *Authorea Preprints*.
- Hersbach, H., Bell, B., Berrisford, P., Hirahara, S., Horányi, A., Muñoz-Sabater, J., et al. (2020). The ERA5 global reanalysis. *Quarterly Journal of the Royal Meteorological Society*, 146(730), 1999–2049. <https://doi.org/10.1002/qj.3803>
- Hirons, L., Klingaman, N., & Woolnough, S. (2018). The impact of air–sea interactions on the representation of tropical precipitation extremes. *Journal of Advances in Modeling Earth Systems*, 10(2), 550–559. <https://doi.org/10.1002/2017ms001252>
- Holland, P. R., & Kwok, R. (2012). Wind-driven trends in Antarctic sea-ice drift. *Nature Geoscience*, 5(12), 872–875. <https://doi.org/10.1038/ngeo1627>
- Huang, B., Thorne, P. W., Banzon, V. F., Boyer, T., Chepurin, G., Lawrimore, J. H., et al. (2017). Extended reconstructed sea surface temperature, version 5 (ERSSTv5): Upgrades, validations, and intercomparisons. *Journal of Climate*, 30(20), 8179–8205. <https://doi.org/10.1175/jcli-d-16-0836.1>
- Janssen, P. A. (1989). Wave-induced stress and the drag of air flow over sea waves. *Journal of Physical Oceanography*, 19(6), 745–754. [https://doi.org/10.1175/1520-0485\(1989\)019<0745:wisatd>2.0.co;2](https://doi.org/10.1175/1520-0485(1989)019<0745:wisatd>2.0.co;2)
- Janssen, P. A. (1991). Quasi-linear theory of wind-wave generation applied to wave forecasting. *Journal of Physical Oceanography*, 21(11), 1631–1642. [https://doi.org/10.1175/1520-0485\(1991\)021<1631:qltoww>2.0.co;2](https://doi.org/10.1175/1520-0485(1991)021<1631:qltoww>2.0.co;2)
- Janssen, P. A. (2004). *The interaction of ocean waves and wind*. Cambridge University Press.
- Kaspi, Y., & Schneider, T. (2011). Winter cold of eastern continental boundaries induced by warm ocean waters. *Nature*, 471(7340), 621–624. <https://doi.org/10.1038/nature09924>
- Lee, J., Planton, Y. Y., Gleckler, P. J., Sperber, K. R., Guilyardi, E., Wittenberg, A. T., et al. (2021). Robust evaluation of ENSO in climate models: How many ensemble members are needed? *Geophysical Research Letters*, 48(20), e2021GL095041. <https://doi.org/10.1029/2021gl095041>
- Li, Q., Fox-Kemper, B., Breivik, Ø., & Webb, A. (2017). Statistical models of global langmuir mixing. *Ocean Modelling*, 113, 95–114. <https://doi.org/10.1016/j.ocemod.2017.03.016>
- Li, Q., Webb, A., Fox-Kemper, B., Craig, A., Danabasoglu, G., Large, W. G., & Vertenstein, M. (2016). Langmuir mixing effects on global climate: WAVEWATCH III in CESM. *Ocean Modelling*, 103, 145–160. <https://doi.org/10.1016/j.ocemod.2015.07.020>
- Li, Z., Fung, J. C., Wong, M. F., Lin, S., Cai, F., Lai, W., & Lau, A. K. (2024). Future changes in intense tropical cyclone hazards in the pearl river delta region: An air-wave-ocean coupled model study. *Natural Hazards*, 120(8), 7139–7154. <https://doi.org/10.1007/s11069-024-06510-7>
- Lin, S., & Sheng, J. (2020). Revisiting dependences of the drag coefficient at the sea surface on wind speed and sea state. *Continental Shelf Research*, 207, 104188. <https://doi.org/10.1016/j.csr.2020.104188>
- Lin, S., Sheng, J., Ohashi, K., & Song, Q. (2021). Wave-current interactions during hurricanes earl and igor in the northwest atlantic. *Journal of Geophysical Research: Oceans*, 126(12), e2021JC017609. <https://doi.org/10.1029/2021jc017609>
- Liu, B., Guan, C., Xie, L., & Zhao, D. (2012). An investigation of the effects of wave state and sea spray on an idealized typhoon using an air-sea coupled modeling system. *Advances in Atmospheric Sciences*, 29(2), 391–406. <https://doi.org/10.1007/s00376-011-1059-7>
- Liu, J., Curry, J. A., Clayson, C. A., & Bourassa, M. A. (2011). High-resolution satellite surface latent heat fluxes in North Atlantic hurricanes. *Monthly Weather Review*, 139(9), 2735–2747. <https://doi.org/10.1175/2011mwr3548.1>
- Luongo, M. T., Brizuela, N. G., Eisenman, I., & Xie, S.-P. (2024). Retaining short-term variability reduces mean state biases in wind stress overriding simulations. *Journal of Advances in Modeling Earth Systems*, 16(2), e2023MS003665. <https://doi.org/10.1029/2023ms003665>
- Mogensen, K. S., Magnusson, L., & Bidlot, J.-R. (2017). Tropical cyclone sensitivity to ocean coupling in the ECMWF coupled model. *Journal of Geophysical Research: Oceans*, 122(5), 4392–4412. <https://doi.org/10.1002/2017jc012753>
- Neale, R. B., Chen, C.-C., Gettelman, A., Lauritzen, P. H., Park, S., Williamson, D. L., et al. (2010). Description of the NCAR community atmosphere model (CAM 5.0). *NCAR Technical Note NCAR/TN-486+STR*, 1(1), 1–12.
- Newman, M., Sardeshmukh, P. D., & Penland, C. (2009). How important is air–sea coupling in enso and mjo evolution? *Journal of Climate*, 22(11), 2958–2977. <https://doi.org/10.1175/2008jcli2659.1>
- Nilsson, E. O., Rutgereson, A., Smedman, A.-S., & Sullivan, P. P. (2012). Convective boundary-layer structure in the presence of wind-following swell. *Quarterly Journal of the Royal Meteorological Society*, 138(667), 1476–1489. <https://doi.org/10.1002/qj.1898>
- Olabarrieta, M., Warner, J. C., Armstrong, B., Zamboni, J. B., & He, R. (2012). Ocean-atmosphere dynamics during hurricane IDA and NOR’IDA: An application of the coupled ocean-atmosphere-wave-sediment transport (COAWST) modeling system. *Ocean Modelling*, 43, 112–137. <https://doi.org/10.1016/j.ocemod.2011.12.008>
- OSI SAF. (2022). Global sea ice concentration climate data record v3.0—Multimission, EUMETSAT SAF on ocean and sea ice. [https://doi.org/10.15770/EUM\\_SAF\\_OSI\\_0013](https://doi.org/10.15770/EUM_SAF_OSI_0013)
- Pianezze, J., Barthe, C., Bielli, S., Tuleit, P., Jullien, S., Cambon, G., et al. (2018). A new coupled ocean-waves-atmosphere model designed for tropical storm studies: Example of tropical cyclone Bejisa (2013–2014) in the south-west Indian Ocean. *Journal of Advances in Modeling Earth Systems*, 10(3), 801–825. <https://doi.org/10.1002/2017ms001177>
- Potter, H. (2015). Swell and the drag coefficient. *Ocean Dynamics*, 65(3), 375–384. <https://doi.org/10.1007/s10236-015-0811-4>
- Prakash, K. R., Pant, V., & Nigam, T. (2019). Effects of the sea surface roughness and sea spray-induced flux parameterization on the simulations of a tropical cyclone. *Journal of Geophysical Research: Atmospheres*, 124(24), 14037–14058. <https://doi.org/10.1029/2018jd029760>

- Qiao, F., Song, Z., Bao, Y., Song, Y., Shu, Q., Huang, C., & Zhao, W. (2013). Development and evaluation of an earth system model with surface gravity waves. *Journal of Geophysical Research: Oceans*, 118(9), 4514–4524. <https://doi.org/10.1002/jgrc.20327>
- Reguero, B. G., Losada, I. J., & Méndez, F. J. (2019). A recent increase in global wave power as a consequence of oceanic warming. *Nature Communications*, 10(1), 205. <https://doi.org/10.1038/s41467-018-08066-0>
- Reichl, B. G., Hara, T., & Ginis, I. (2014). Sea state dependence of the wind stress over the ocean under hurricane winds. *Journal of Geophysical Research: Oceans*, 119(1), 30–51. <https://doi.org/10.1002/2013jc009289>
- Rutgersson, A., Nilsson, E., & Kumar, R. (2012). Introducing surface waves in a coupled wave-atmosphere regional climate model: Impact on atmospheric mixing length. *Journal of Geophysical Research*, 117(C11), C00J15. <https://doi.org/10.1029/2012jc007940>
- Seager, R., Henderson, N., & Cane, M. (2022). Persistent discrepancies between observed and modeled trends in the tropical pacific ocean. *Journal of Climate*, 35(14), 4571–4584. <https://doi.org/10.1175/jcli-d-21-0648.1>
- Semedo, A., Sušelj, K., Rutgersson, A., & Sterl, A. (2011). A global view on the wind sea and swell climate and variability from era-40. *Journal of Climate*, 24(5), 1461–1479. <https://doi.org/10.1175/2010jcli3718.1>
- Shi, X. (2025a). Data for “The effects of sea-state-dependent surface fluxes on CESM2 climate simulations” [Dataset]. *Zenodo*. <https://doi.org/10.5281/zenodo.15593559>
- Shi, X. (2025b). Modified CESM2 components for sea-state dependent surface fluxes [Software]. *Zenodo*. <https://doi.org/10.5281/zenodo.17066443>
- Shimura, T., Mori, N., Takemi, T., & Mizuta, R. (2017). Long-term impacts of ocean wave-dependent roughness on global climate systems. *Journal of Geophysical Research: Oceans*, 122(3), 1995–2011. <https://doi.org/10.1002/2016jc012621>
- Simpson, I. R., Bacmeister, J. T., Sandu, I., & Rodwell, M. J. (2018). Why do modeled and observed surface wind stress climatologies differ in the trade wind regions? *Journal of Climate*, 31(2), 491–513. <https://doi.org/10.1175/jcli-d-17-0255.1>
- Song, Z., Qiao, F., & Song, Y. (2012). Response of the equatorial basin-wide SST to non-breaking surface wave-induced mixing in a climate model: An amendment to tropical bias. *Journal of Geophysical Research*, 117(C11), 247. <https://doi.org/10.1029/2012jc007931>
- Taylor, P. K., & Yelland, M. J. (2001). The dependence of sea surface roughness on the height and steepness of the waves. *Journal of Physical Oceanography*, 31(2), 572–590. [https://doi.org/10.1175/1520-0485\(2001\)031<0572:tdossr>2.0.co;2](https://doi.org/10.1175/1520-0485(2001)031<0572:tdossr>2.0.co;2)
- Turner, J., Guarino, M. V., Arnatt, J., Jena, B., Marshall, G. J., Phillips, T., et al. (2020). Recent decrease of summer sea ice in the Weddell sea, Antarctica. *Geophysical Research Letters*, 47(11), e2020GL087127. <https://doi.org/10.1029/2020gl087127>
- Vallis, G. K. (2017). *Atmospheric and oceanic fluid dynamics*. Cambridge University Press.
- Wada, A., Kanada, S., & Yamada, H. (2018). Effect of air-sea environmental conditions and interfacial processes on extremely intense typhoon Haiyan (2013). *Journal of Geophysical Research: Atmospheres*, 123(18), 10–379. <https://doi.org/10.1029/2017jd028139>
- Warner, J. C., Armstrong, B., He, R., & Zambon, J. B. (2010). Development of a coupled ocean–atmosphere–wave–sediment transport (COAWST) modeling system. *Ocean Modelling*, 35(3), 230–244. <https://doi.org/10.1016/j.ocemod.2010.07.010>
- Wills, R. C., Dong, Y., Proistosescu, C., Armour, K. C., & Battisti, D. S. (2022). Systematic climate model biases in the large-scale patterns of recent sea-surface temperature and sea-level pressure change. *Geophysical Research Letters*, 49(17), e2022GL100011. <https://doi.org/10.1029/2022gl100011>
- Wu, L., Rutgersson, A., & Nilsson, E. (2017). Atmospheric boundary layer turbulence closure scheme for wind-following swell conditions. *Journal of the Atmospheric Sciences*, 74(7), 2363–2382. <https://doi.org/10.1175/jas-d-16-0308.1>
- Wu, L., Sahlée, E., Nilsson, E., & Rutgersson, A. (2024). A review of surface swell waves and their role in air-sea interactions. *Ocean Modelling*, 190, 102397. <https://doi.org/10.1016/j.ocemod.2024.102397>
- Young, I. R. (1999). Seasonal variability of the global ocean wind and wave climate. *International Journal of Climatology*, 19(9), 931–950. [https://doi.org/10.1002/\(sici\)1097-0088\(199907\)19:9<931::aid-joc412>3.0.co;2-o](https://doi.org/10.1002/(sici)1097-0088(199907)19:9<931::aid-joc412>3.0.co;2-o)
- Yu, H., Chen, P., Li, Q., & Tang, B. (2013). Current capability of operational numerical models in predicting tropical cyclone intensity in the western north pacific. *Weather and Forecasting*, 28(2), 353–367. <https://doi.org/10.1175/waf-d-11-00100.1>
- Zhao, B., Wang, G., Zhang, J. A., Liu, L., Liu, J., Xu, J., et al. (2022). The effects of ocean surface waves on tropical cyclone intensity: Numerical simulations using a regional atmosphere-ocean-wave coupled model. *Journal of Geophysical Research: Oceans*, 127(11), e2022JC019015. <https://doi.org/10.1029/2022jc019015>
- Zhu, J., & Shukla, J. (2013). The role of air–sea coupling in seasonal prediction of Asia–Pacific summer monsoon rainfall. *Journal of Climate*, 26(15), 5689–5697. <https://doi.org/10.1175/jcli-d-13-00190.1>